



Zebra dolomites of the Spessart, Germany: implications for hydrothermal systems of the European Zechstein Basin

Ulrich Kelka¹ · Nicolas E. Beaudoin² · Joachim Lorenz³ · Daniel Koehn⁴ · Klaus Regenauer-Lieb⁵ · Adrian Boyce⁶ · Peter Chung⁷

Received: 4 April 2022 / Accepted: 11 September 2023 / Published online: 25 October 2023
© The Author(s) 2023

Abstract

Zebra dolomites have a distinctive texture and are a peculiar structural variety of dolostones often encountered in the vicinity of base metal deposits commonly in the Mississippi Valley-Type (MVT). We investigate origin and evolution of the zebra dolomites found in the region of the Spessart, northwestern Bavaria, Germany, through diagenetic and petrogenetic analysis using SEM, CL microscopy, *O*–*C* isotopes, and fluid inclusion micro-thermometry. Here, we aim to shed light on the nature of the fluids that altered the zebra dolomite of the Zechstein formation. We distinguish the geochemical signatures of two different fluid flow regimes post-dating texture formation, each characterized by specific homogenization temperatures and oxygen–carbon isotope ratios (Event 1: $T_h = 120$ °C; $\delta^{18}O_{\text{fluids}} = [0 \text{ to } 2\text{‰}]$; Event 2; $T_h = 300$ °C; $\delta^{18}O_{\text{fluids}} = 18\text{‰}$). Comparison of these fluids and the associated mineralization with published regional fluid flow data support that the zebra dolomites in the Spessart most likely coincided with the Permian large-scale fluid flow event that occurred throughout the European Zechstein Basin.

Keywords Zebra dolomites · Spessart · Hydrothermal systems · Dolomitization · Dedolomitization

Introduction

The formation of base metal deposits is often related to regional-scale, fluid–rock interactions that involve large volumes of reactive fluids (e.g., Blundell et al. 2003). The classification of such ore deposits is based on the host rock mineralogy and the source of fluids, either hydrothermal or magmatic in origin, and whether the ore formation is associated with surficial processes, such as weathering, sedimentation, or chemical precipitation (Dill 2010). Nearly all economic Pb, Zn, and Mo deposits were formed by hydrothermal activity (Arndt and Ganino 2012). Within the class of hydrothermal deposits, different types can be distinguished. Well-known examples of basinal hydrothermal systems are sedimentary exhalative deposits (SEDEX) and MVT. The latter are defined as epigenetic, strata-bound sulfide deposits hosted in carbonates, and account for 38% of the worldwide Pb–Zn resources in sedimentary-hosted ore deposits (Leach et al. 2010).

Carbonates hosting MVT deposits frequently exhibit replacive dolomite often with periodic alternation between dark and white dolomite crystal layers: the zebra dolomite (Beales and Jackson 1968; Radke and Mathis 1980; Fontboté

✉ Ulrich Kelka
ukelka@yahoo.de

¹ CSIRO, Mineral Resources, 26 Dick Perry Ave, Kensington, WA 6151, Australia

² Universite de Pau et des Pays de l'Adour, E2S UPPA, CNRS, Total Energies, LFCR, Pau, France

³ Graslitzer Str. 5, 63791 Karlstein a. Main, Germany

⁴ FAU University Erlangen Nuremberg, Geozentrum Nordbayern, Erlangen, Germany

⁵ WA School of Mines: Minerals, Energy and Chemical Engineering, Curtin University, Kensington, WA 6151, Australia

⁶ NERC Isotope Community Support Facility, SUERC Rankine Avenue East Kilbride, Glasgow G75 0QF, Scotland, UK

⁷ School of Geographical and Earth Sciences, University of Glasgow, Gregory Building, Glasgow G12 8QQ, Scotland, UK

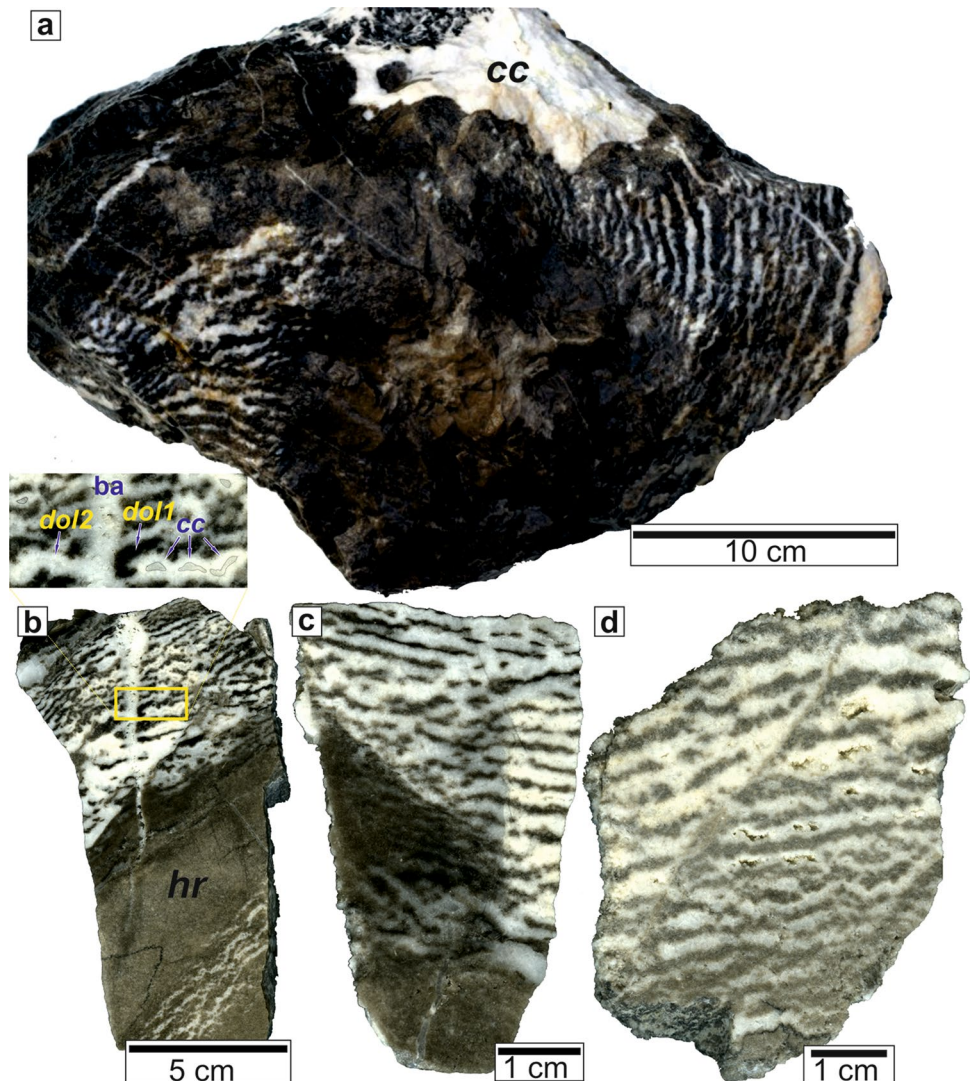
and Amstutz 1982; Fontboté and Gorzawski 1990; Zeeh 1995; Swennen et al. 2003; Vandeginste et al. 2005; Aydal et al. 2008; Diehl et al. 2010; Iriarte et al. 2012; Morrow 2014). Zebra dolomites (Fig. 1) were described worldwide (Fontboté and Amstutz 1982; Fontboté and Gorzawski 1990; Nielsen et al. 1998; Wallace et al. 1994; Zeeh 1995; Vandeginste et al. 2005; Aydal et al. 2008; López Horgue et al. 2009; Diehl et al. 2010; Lopez-Horgue et al. 2010; Liu et al. 2014; Morrow 2014), and share common textural features: the dark bands comprise small crystals and are rich in impurities (secondary mineral phases) (Kelka et al. 2015), while the light bands comprise coarse crystals exhibiting a syntaxial texture, with a median line showing vuggy porosity (i.e., Gasparrini et al. 2006; Wallace and Hood 2017) commonly filled by late-stage carbonate cement (Fig. 1b). Similar textures were described in carbonate formations dominated by siderite (Palinkaš et al. 2009), but have also been observed in sphalerite (Fontboté et al. 1982), barite (Thomassen 2007), fluorite (Wallace et al. 1994), and magnesite (Lugli et al.

2000). These observations, along with the observation of the spatial and temporal relationship that zebra dolomites share with MVT deposits, led for example Merino et al. (2011) to propose that fluids that exhibit a typical composition of MVT-brines trigger the genesis of the zebra pattern in dolomites.

However, there has been a long-standing debate on how the zebra pattern forms and what processes are responsible for their formation (Badoux et al. 2001; Merino et al. 2006; Lopez-Horgues et al. 2010; Merino and Canal 2011; Vandeginste et al. 2012; Morrow 2014; Kelka et al. 2015, 2017). One view is that the dark and light layers are interpreted as different generations of dolomite that formed in a fluid-saturated rock in an over-pressurized fluid system (Nielsen et al. 1998; Swennen et al. 2003, 2012; Vandeginste et al. 2005). Another view is that the dark layers represent replacive dolomite, while the white layers represent fractures that formed either by tectonic stress (Wallace et al. 1994), overprinting an initial sedimentary structure (Morrow 2014), are

Fig. 1 Zebra dolomite specimen collected from the Falkenberg tunnel. The sample clearly shows that the orientation of the zebra layers can change on a small scale. In this hand specimen, the orientation changes by 90° at the scale of a decimeter. The white patch on top of the sample consists of calcite.

b Hand specimen of a zebra dolomite patch that is crosscut by a vertical barite vein. A clear difference in color between the dolomitic host rock (hr) and the dark zebra layers (dol1) can be observed. The detailed view of the area indicated by the yellow rectangle shows that a calcite phase (cc) precipitated in the central part of the light zebra layers (dol2). [hr is hardly visible, dol1 and dol2 not at all!]. **c** Zebra dolomite that exhibits an alteration post-dating the formation of the structure. In the left part, the pattern looks “washed-out” and especially in the lower part of the sample was replaced by calcite. **d** In this hand specimen, the dolostone was subjected to a strong hydrothermal alteration after the zebra pattern had been formed. The result is a friable rock that exhibits voids along the central parts of the light zebra layers



a function of fluid overpressure (Swennen et al. 2012), or formed by a complex process of vein formation and associated crystallization stress (Merino et al. 2006; Merino and Canals 2011). Other authors propose that recrystallization processes can lead to the development of the zebra pattern as a result of hydro-mechanical material instabilities that form because of the volumetric compaction of fluid-filled, low-permeable rocks (Kelka et al. 2015, 2017). Recently, a combination of mineral replacement and subsequent dissolution has been suggested to be the main mechanism for the pattern formation and the equidistant spacing is thought to be caused by stress shadows associated with the crystallization pressure of the growing carbonate crystals (Wallace and Hood 2018).

In this contribution, we describe and investigate zebra dolomites from the Spessart (NW Bavaria, Germany) in the Central European Zechstein Basin during the Upper Permian Werra Cycle. These zebra dolomites overlie black shales of the *Kupferschiefer*, a strata-bound Cu–Pb–Zn–(Ag) deposit that likely was mineralized by a combination of sedimentary–diagenetic and hydrothermal processes (Wagner et al. 2010). We aim to decipher paragenetic and diagenetic sequences of fluid–rock interaction related to the zebra dolomite formation. The zebra dolostone samples were analyzed petro-graphically using transmitted light, cathodo-luminescence, and scanning electron microscopy with energy-dispersive spectrum (SEM–EDS). The

petrographic characterization was complemented by a fluid inclusion micro-thermometry study and stable isotope analysis to characterize the nature of the fluids trapped within the zebra dolomite.

Geological overview

The Spessart region has been subject to Variscan and post-Variscan deformational phases. The Variscan deformation affected the basement rocks during metamorphism and led to the formation of folds with NE–SW trending axis, overprinted by secondary ESE-trending folds (Cramer et al. 1978). A quartz diorite–granodiorite pluton is linked to a younger tectonic event that was not affected by folding but was accommodated by pre-existing structures (Okrusch and Weinelt 1965). Near the locality of Hain (Fig. 2), at least two small crests formed in basement diorite that represent the sedimentation base of the discordantly overlying Zechstein group (Cramer et al. 1978).

Post-Variscan tectonics are characterized by high-angle normal faults striking NW–SE affecting all successions up to and including the Lower Triassic Bunter group. The different Variscan and post-Variscan deformation phases are important for the precipitation of barite mineralization, which is evident by the presence of barite mineralization in joints related to these different phases (Cramer 1978).

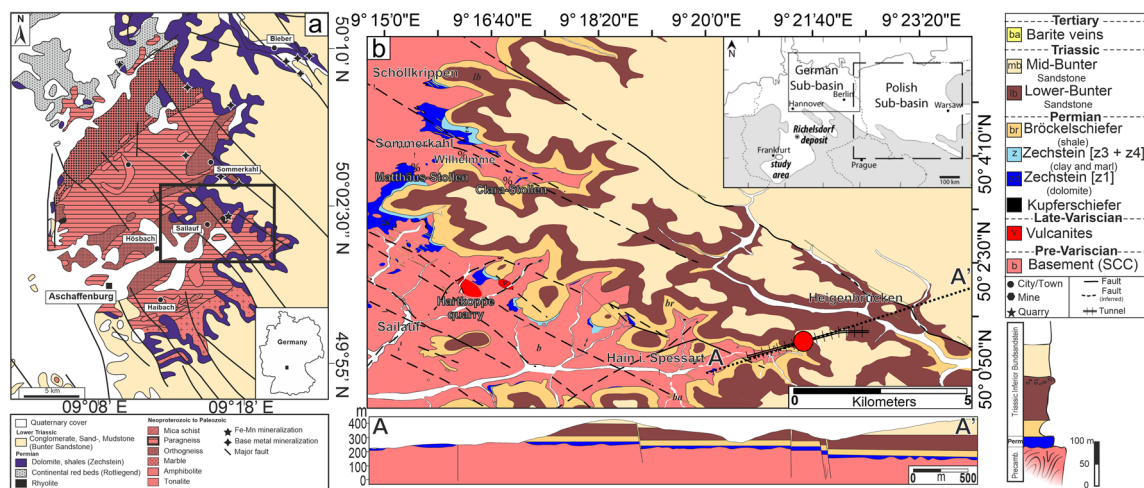


Fig. 2 Left: The map shows the crystalline basement of the Vorpessart, overlain by carbonate sediments of the Upper Permian Zechstein group and Lower Triassic Bunter sandstone. The black rectangle indicates the location of the detailed geological map to the right (map modified after Wagner et al. 2010). Right: Detailed geological overview of the area around the Falkenberg Tunnel. The tunnel dives from the crystalline Vorpessart into the Triassic Sediments of the Hochspessart. The cross-sectional A–A' is oriented parallel to the tunnel whereas the location of the zebra dolomites in the tunnel is indicated by a rectangular zebra pattern. At the margin of these two units several phases of mineralization are encountered that are spa-

tially linked to the Kupferletten, the equivalent to the Kupferschiefer in the Spessart district. The lithological profile to right shows where the Zechstein formation is located with respect to the basement and the overlying Triassic successions. (Map modified after Okrusch and Weinelt 1965; Cramer and Weinelt 1975; Wagner et al. 2010; Fusswinkel et al. 2014). The schematic overview in the top right corner of the map shows the extension of the Zechstein basin (white), the location of the Richesdorf Kupferschiefer-deposit and the locations of the Zechstein samples in the German sub-basin (A) and the Polish sub-basin (B) that had been investigated by Schmidt-Mumm et al. (2004). Map had been modified after Alderton et al. (2012)

In the Spessart region, barite mineralization occurred post-Variscan during the Jurassic to Tertiary (Okrusch et al. 2007; Okrusch and Weinelt 1965; Okrusch et al. 2007; Wagner et al. 2010; Walther 2012).

It is important to differentiate between basement joints that are associated with the folding of the crystalline basement and the jointing in overlying sedimentary rocks. The fold-related joints in the basement do not continue into the overlying sedimentary rocks, while the joint orientations in the Zechstein and Bunter formations have similarities. Two sets of joints can be distinguished within the Zechstein: one barite bearing set striking 120° – 150° and one barren set striking predominantly 30° – 50° , while a minor strike of 70° was also observed for this set. Differences in joint orientations between the Zechstein and Bunter formations are likely attributed to the mechanical buffering of the Bröckelschiefer formation occurring between these two strata (Okrusch and Weinelt 1965).

The post-Variscan extension led to the reactivation of fault-related fluid systems resulting in a variety of mineralization types. Barite mineralization phases of different ages are documented throughout the Spessart and are evidence for the occurrence of several hydrothermal fluid flow events. An extensive large-scale upward migration of hydrothermal fluids led to the precipitation of sulfides and arsenides in locally economically significant proportions and occurred predominantly during the Mid-Jurassic to Cretaceous (Okrusch et al. 2007 and references therein). On the scale of the Zechstein basin, the underlying basin fluid system, which extended over a large area of Europe, is temporally associated with the extension and subsidence of the basin (Schmidt-Mumm and Wolfgramm 2004).

The Spessart represents the southwestern margin of the Permian Kupferschiefer basin (Ziegler 1990; Wagner et al. 2010) that was part of a WNW–ESE striking intercontinental Permian Basin (PB). The PB was part of northern Pangea and formed in the Late Carboniferous to Early Permian (Słowakiewicz et al. 2018) due to rifting-related subsidence (Gast 1988). The extension of the basin resulted in widespread volcanic activity throughout Europe that led to the deposition of volcanoclastic sequences and the emplacement of plutons (Okrusch et al. 2011). As the basin contained the epicontinental Zechstein Sea, it is also referred to as the Zechstein Basin, which was subject to a series of marine transgression and regression cycles. These resulted in the cyclical deposition of marine sediments, such as carbonates, marls, and evaporites (Zechstein series z1–z7).

On a regional scale, the Spessart can be subdivided mineralogically into the Spessart Crystalline Complex (SCC) located in the Vorspessart, and the overlying Bunter Sandstone, which are represented by thick sandstone units of Lower Triassic age located in the Hochspessart (e.g., Okrusch and Weber 1996; Okrusch et al. 2011). The SCC consists

of SW–NE trending meta-sedimentary and meta-igneous units, which have been metamorphosed to mid-amphibolite facies and intruded by a quartz diorite–granodiorite pluton. The SCC is part of the Mid-German Crystalline Rise, an internal zone of the European Variscides (e. g. Dombrowski et al. 1995; Okrusch and Richter 1986; Okrusch and Weber 1996; Okrusch et al. 2011; Will et al. 2015; Fig. 2). The zebra dolomites analyzed in this study formed in Zechstein carbonates situated at the boundary between the SSC and the Bunter Sandstone (Fig. 2). A lithological profile (Fig. 2) shows where the Zechstein formation hosting zebra textures are located with respect to the basement and the overlying Triassic successions.

When the Zechstein carbonates were deposited during the Upper Permian, the Spessart was located in the Hessian depression within the German sub-basin at the southern edge of the Zechstein Sea. The marginal facies of the Zechstein basin was characterized by a high concentration of carbonates and fine-grained clastic material (e.g., Vaughan et al. 1989; Wagner et al. 2010; Okrusch et al. 2011; Fusswinkel et al. 2014). This carbonate sequence hosts the zebra dolomites (Figs. 1, 3). A basal breccia or conglomerates, marls, shale, and dolomites [Zechstein z1–Werra cycle] usually mark the beginning of the Zechstein cycle (Käding 2005).

Regional mineralization history

The formation of the zebra dolomites is linked to hydrothermal alteration and potential mineralization. In the Spessart, several mineralization types can be distinguished (Wagner et al. 2010) and here we describe the types of mineralisation that are found in the vicinity of the zebra dolomite occurrence in the Falkenberg tunnel. Economically, the most significant ore deposits in the vicinity are the Kupferschiefer deposits which are one of the world's largest and arguably most famous copper enrichments of this type (Schmidt and Friedrich 1988). The name of the deposit is derived from the Permian Kupferschiefer Formation, which consists of clay-rich bituminous shale that was deposited on the floor of the Zechstein Sea, probably under reducing conditions. The marginal facies of the Kupferschiefer can reach a thickness of up to 4 m, whereas the thickness of the basal facies is typically 0.3–0.5 m (Vaughan et al. 1989 and references therein). The metal enrichment associated with the Kupferschiefer formation is not restricted to this stratigraphic unit but also spreads into Zechstein sedimentary rocks (Borg et al. 2012). Base metals are concentrated predominantly in the basal part of the Kupferschiefer with dominant ore minerals being Cu–As sulfides (tennantite, enargite) and arsenides (loellingite, arsenopyrite) replacing older copper sulfides (Vaughan et al. 1989 and references therein). Additional mineralization occurs as strata-bound mineralization (Cu–Pb–Zn–(Ag)–As) hosted mainly by the Kupferschiefer

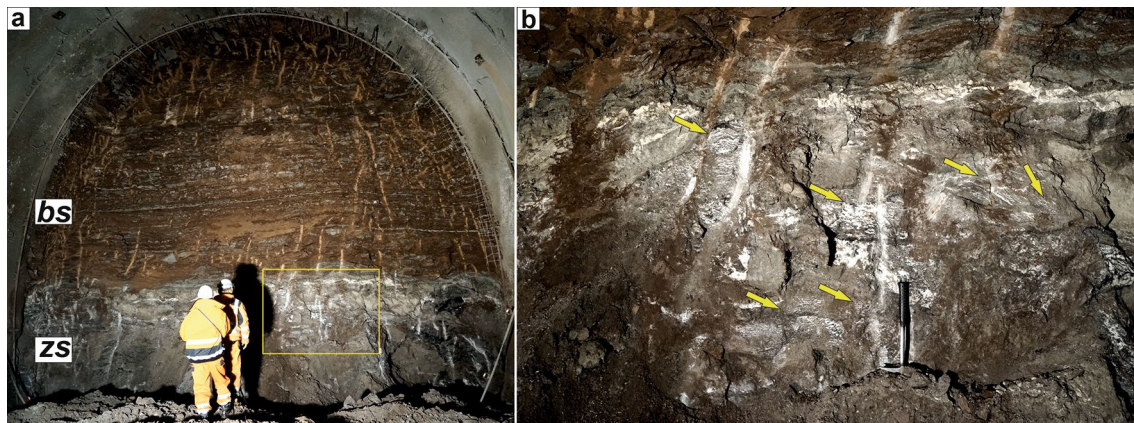


Fig. 3 **a** Outcrop of the Zechstein carbonates (zs) hosting zebra dolomites in the Falkenberg tunnel approximately 1074 m from the western entrance of the tunnel in the left track. The Zechstein dolomite exhibits a wavy contact with the overlying clay-rich Bröckelschiefer (bs). **b** Detailed view of the area marked by the yellow rectangle in Fig. 2a. The zebra pattern occurs in the form of isolated patches (indi-

cated by the yellow arrows). Most of the zebra layers are orientated parallel to the bedding planes of the overlying Bröckelschiefer but in some areas the layering is at an angle of about 45° to the bedding. Apart from the zebra patches numerous light regions can be observed that are filled with calcite and/or barite indicating a hydrothermal alteration that affected the sedimentary strata

unit and adjacent carbonates (Wagner et al. 2010). Epigenetic polymetallic veins (Co, Ni, Bi, As sulfides) are predominantly hosted by the Zechstein carbonates (Wagner and Lorenz 2002; Okrusch et al. 2007) and in the underlying Permian redbeds, which is considered to be one source of the base metals (i.e., Jowett 1986) that were leached by upwelling hydrothermal fluids and precipitated at shallower depths (Borg et al. 2012). Copper was likely leached by the same hydrothermal fluids from abundant volcanoclastic lithologies in the lower part of the redbeds (Borg et al. 2012). It is thought that the Cu deposition was probably triggered by reducing organic matter contained in the Kupferschiefer formation. The exact timing of the mineralization is still controversial today (Jowett 1986; Fusswinkel et al. 2014).

Relicts of the primary Kupferschiefer mineralization stage are preserved sporadically in the Spessart as most of the earlier deposits have been reworked and remobilized by subsequent fluid flow events (Wagner et al. 2010). Different mineralization stages are thought to result from the episodic release of hydrothermal fluids related to the extension and subsidence of the Permian Basin that continued at least until the Cretaceous (Alderton et al. 2016). Schmidt-Mumm and Wolfgramm (2004) observed that the evolution of the fluid system that formed the Kupferschiefer-type mineralization is coherent on a regional scale and is related to the tectonic evolution of the southern Permian Basin.

Near the Falkenberg tunnel, four distinct types of mineralization are of importance (Fig. 2). The tectonically controlled vein-type mineralization (type 1), hosted by metamorphic rocks of the SCC is Mid-Jurassic to late Cretaceous in age. As this type of deposit often shows a close spatial relationship to the strata-bound Cu–Zn–Pb mineralization of

the Upper Permian Kupferschiefer, a genetic link between both metal enrichments is likely (Okrusch et al. 2007). Metasomatic strata-bound Fe–Mn mineralization (type 2) occurs throughout the Spessart and formed within the Zechstein formation, above the Kupferschiefer and below the Bröckelschiefer units (Okrusch et al. 2007). A hydrothermal origin is likely for this mineralization given the spatial correlation of the mineralization to faults, the brecciation of ore zones, the presence of Ba-bearing veins, as well as the sporadic silicification of associated dolomite (Okrusch and Weinelt 1965).

The Permian extension of the basin also caused magmatism of which the rhyolite that is exposed in the Hartkoppe quarry to the east of Sailauf is an example in the Spessart (Fig. 2). This rhyolite intrusion hosts a versatile assemblage of hydrothermal Fe–Mn–As minerals (type 3) that are located at the unconformity between the underlying basement and the overlying Zechstein carbonates. Based on geochemical studies, Fusswinkel et al. (2013) distinguished two main ore-forming stages in the Hartkoppe mineralization: stage I comprised cockade ore (braunite), calcite hausmannite and small, needle-shaped manganite and bixbyite; stage II is characterized by the formation of Mn calcite and the subsequent precipitation of Fe–Mg calcite. The mineralization is concluded by an alteration stage that comprises several replacement mineral phases (Fusswinkel et al. 2013). The mineralization is interpreted to have resulted from two periods of hydrothermal fluid flow, one dominated by the precipitation of Mn oxide and the other by hematite. The fluids of the Mn oxide stage are comparable to fluids that mineralized fractures in the Permian redbeds, and the fluids that resulted in the hematite stage exhibit compositions

that are similar to basement-derived mineralizing brines as described, for instance, by Muchez et al. (2005) and Fusswinkel et al. (2014). The age of the mineralization was determined by dating of oxide minerals and illite and indicates hydrothermal activity from Mid-Jurassic to Early Cretaceous time (178–180 Ma) (Hautmann et al. 1999; Okrusch et al. 2007).

Barite (type 4) can be traced along major faults throughout the Spessart and occurs as several sets of veins that often follow Hercynian NW–SE strike. Widespread similarities in the mineralogy of these veins provide evidence for a large hydrothermal network that prevailed in deep formations within the basement (Wagner et al. 2010). The relative age of the barite is younger than Triassic (Cramer and Weinelt 1978). The dominant mineralization in the Spessart is spatially related to and constrained by high-permeability zones around faults and was driven by upwelling hydrothermal fluids during the post-Variscan extension of the European basin (Cramer and Weinelt 1978).

Studied samples

The strata that host the zebra texture investigated in this study were only made accessible because of regional railroad development and the construction of the Falkenberg railway tunnel (Lorenz 2018). Zechstein carbonates with zebra textures were encountered approximately at tunnel meter 1100 m along the right track and at tunnel meter 1074 m along the left track (Fig. 2). At the study site, the zebra dolomites unconformably overlie the crystalline basement. Clay-rich bituminous shales of the Kupferschiefer that are thought to be linked to base metal mineralization (Wagner et al. 2009) are sparse in the area and only outcrop sporadically below the Zechstein carbonates along the boundary between the basement and the overlying Permian sedimentary rocks (Fig. 2). The bedding of the dolomite is sub-horizontal and is conformable to the overlying strata, as indicated by the orientation of bedding-parallel stylolites (Fig. 3).

The overlying stratum, the “Bröckelschiefer”, is a low-permeability, clay-rich horizon, forming the Fulda formation of the uppermost Zechstein group (Fig. 3a). Most of the zebra layers are oriented parallel to the bedding planes of the Bröckelschiefer but in some areas, the layering is at an angle of about 45° to the bedding. It is noted that, because of incomplete stratigraphic records, the affiliation of the carbonate succession observed in the Falkenberg tunnel cannot be assigned to a specific cycle within the Zechstein group.

The zebra dolostone occurs as isolated patches (Fig. 2b), where most of the zebra bands run parallel to the bedding plane, yet some bands are oblique to the bedding (Fig. 2b). The orientation of zebra stripes changes significantly (by up to 90°) between different patches of stripes even though these patches are only 10 to 15 cm apart from each other

(Fig. 3a). The spacing between zebra layers also changes at the scale of a hand specimen, from 1 mm to 1 cm (Fig. 3b). Other features of the structure are branching and small displacement of zebra bands that can be observed in Fig. 3b, c.

Methods

Thin sections of different thicknesses were prepared from three representative hand specimens (Fig. 1b–d). We conducted a petrographic, diagenetic, and mineralogical study of the zebra dolomite using transmitted light, cathodoluminescence (CL), and scanning electron microscopy (SEM) in combination with energy-dispersive spectroscopy (EDS) analysis. We also reconstructed the chemical composition and the temperature phase of the past fluids to infer the origin of the fluids that interacted with the rock during and after the pattern development. This was achieved by oxygen and carbon stable isotope analysis coupled with fluid inclusion micro-thermometry of fluid inclusions sampled from both, dolomite and calcite cements in the zebra bands. The petrographic characterization of the samples was performed using a Carl Zeiss Axioplan polarized microscope on 30 µm thick sections (Figs. 4, 5, 6c). A preliminary assessment of chemical variations was performed using Cathodoluminescence CITL CCL 8200 Mk4 instrument operating under constant gun conditions of 15 kV and 300 µA. The microstructural and the chemical mapping of both carbonate and non-carbonate species of the zebra samples were imaged with a Carl Zeiss Sigma VPAnalytical SEM equipped with Oxford Instruments Aztec microanalysis (EDS) at the Imaging Spectroscopy and Analysis Centre at the University of Glasgow (Figs. 7, 8, 9, 10).

Fluid inclusion micro-thermometry was carried out at the University of Glasgow using a Linkam MDS600 heating/freezing stage connected to a TMS94 System Controller equipped with an LNP94/2 liquid nitrogen-cooling pump. The micro-thermometric stage was calibrated with an accuracy of 0.5 °C from 50 to 600 °C, following the protocol established by MacDonald and Spooner (1981). We selected only isolated inclusions or assemblages of primary fluid inclusions on three polished 100 µm-thick sections of which the diagenetic state of the calcite cement was checked by cathodo-luminescence microscopy on mirror sections (Fig. 11a, c). The studied fluid inclusions were biphasic, with a size ranging from 10 to 20 µm. Homogenization temperatures were obtained by ramping up the temperature at a rate of 5 °C/min to the point that the bubble started to move. The heating rate was then decreased to 2 °C/min, with a 2-min hold of the temperature every 4 °C. Given the size of the fluid inclusions and to avoid stretching, the temperature of homogenization was determined by reaching the temperature at which the bubble was no longer visible (with an accuracy of 0.5 °C). The temperature was then decreased

Fig. 4 left: Overview scan of a thin section with clearly observable zebra banding. The central part of the light layers is frequently filled with calcite. Right: **1** composite micrograph (PPL) showing a profile along the whole thin section. The banding is hardly visible, and no considerable grain size difference is observed. **2** Micrograph (XPL) of the area indicated in the scan. Around the calcite cement (cc) the crystal shape of dolomite is preserved. This is also observed in micrograph 3 (XPL). One striking feature is that the crystals around the central void-filling calcite appear clear compared to the rest of the thin section that exhibits an overall high impurity density. The images **4** and **5** represent high-resolution scans of the areas indicated in the overview scan. Numerous peloids that probably represent ooid ghosts can be observed and in addition to that, the grain boundaries in the dark areas of the pattern appear very dark

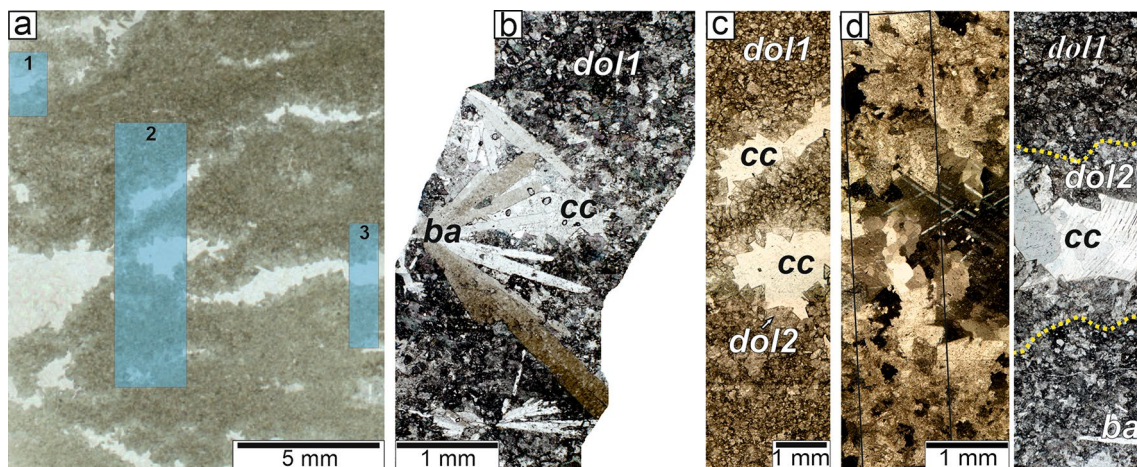
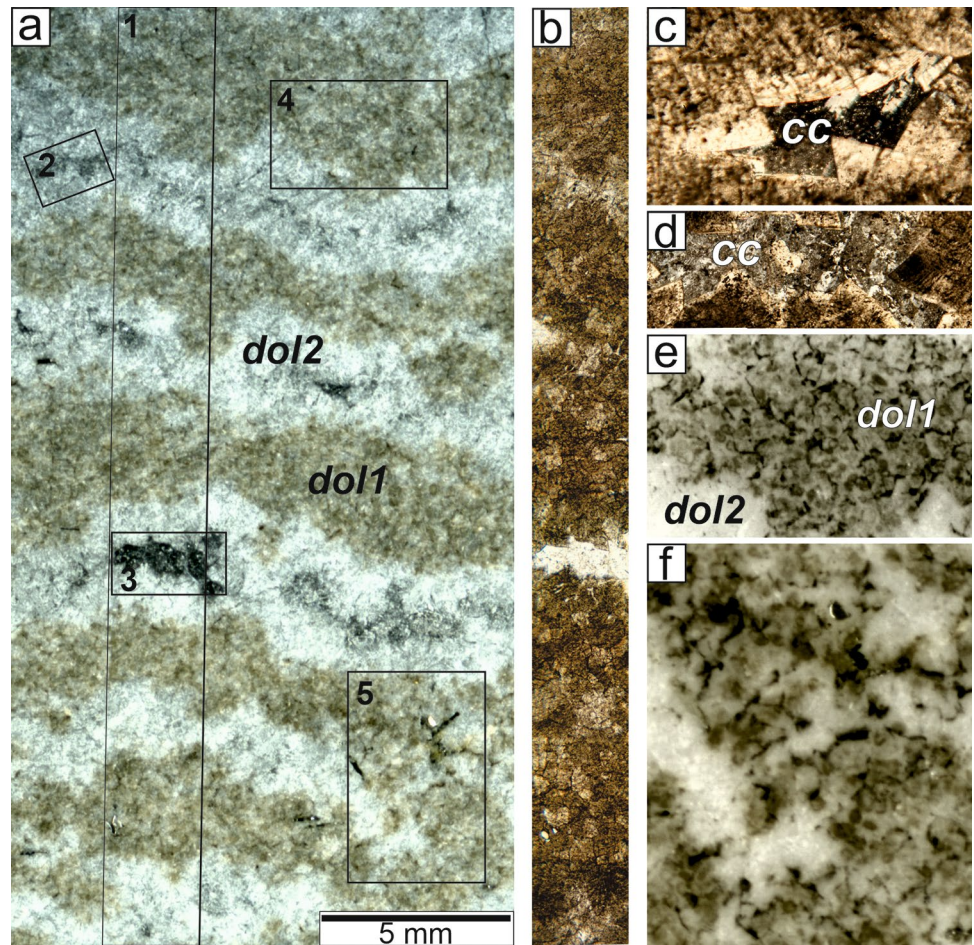


Fig. 5 left: Scan of a highly altered zebra dolomite sample. Right: **1** Micrograph (PPL) shows that the calcite cement (cc) in the central part of the light layers had been overgrown by barite (ba) that is also found in the dark dolomite (dol1). **2** A detailed view (micrograph under PPL) of the banding reveals that the grains surrounding the cal-

cite cement (cc) exhibit the crystal shape of dolomite and comprise a lower impurity concentration compared to the rest of the section. A grain size difference between the dark (dol1) and the light dolomite (dol2) is also observed. In micrograph **3** it is possible to assess the initial border of dol1 and dol2

by 10 °C/min, and this was repeated until the bubble reappeared. When the temperature of homogenization was

reached, the bubble reappeared suddenly, about 40 °C lower than the temperature noted when the bubble disappeared

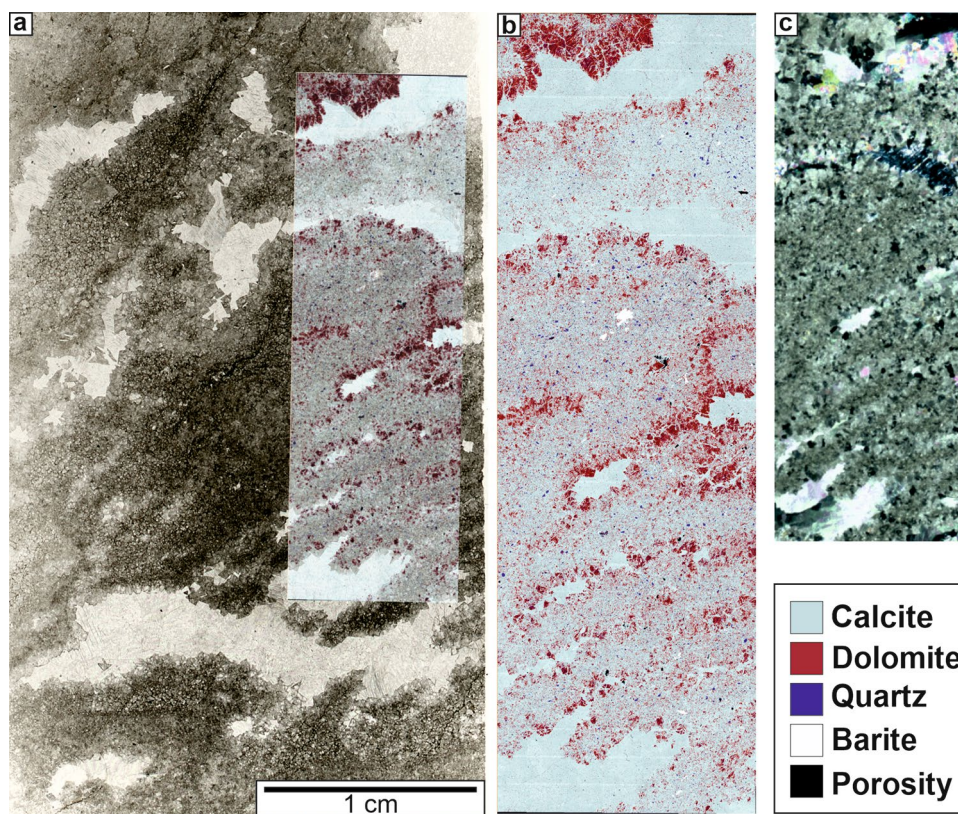


Fig. 6 **a** Scan of altered zebra dolomite samples. Superimposed is a SEM-map (backscattered mode). **b** SEM-map converted into a compositional map. The transformation had been performed with AVIZO based on the greyscale of the initial SEM image. It becomes obvious that the sample had been subjected to extensive dedolomitization, whereas dolomite crystals are still present around the calcite cement in the central parts of light layers. Finely dispersed quartz crystals are present in the dedolomitized dark zebra dolomite layers. **c** micro-

graph (XPL) of the same area shown in **b**. The calcite cement in the central part of the light layers can be clearly distinguished from the rests of the thin section that also consists predominantly of calcite. The microstructure of the calcite cement indicates a void-filling origin indicated by pronounced undulose extinction and curved twinning lamella, which are also observed in the other samples (Figs. 4-2, 4-3, 5-3)

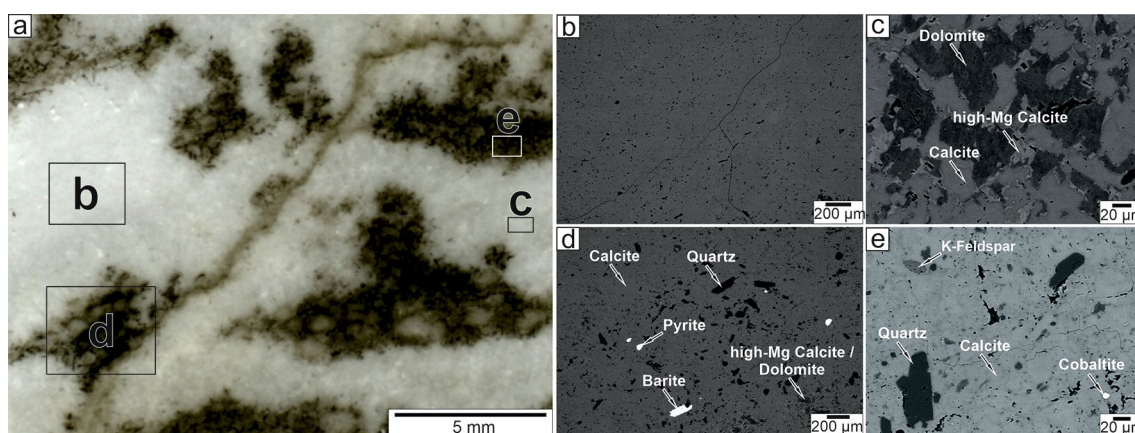
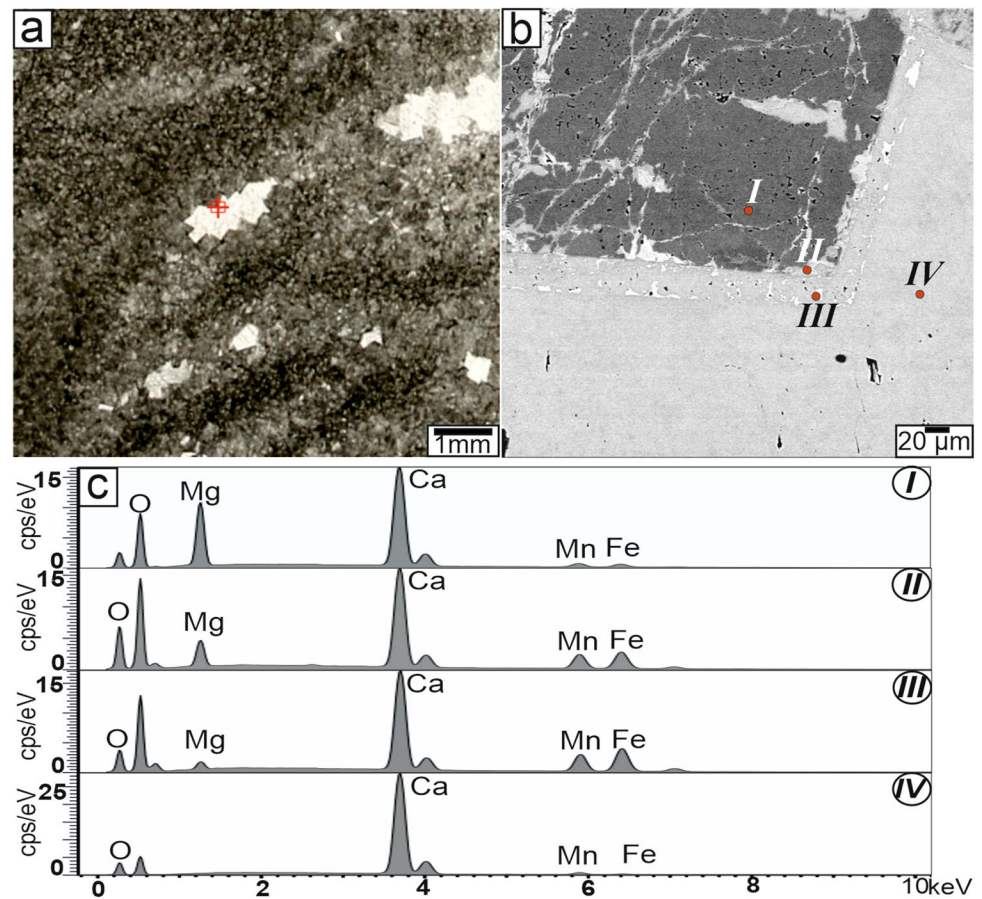


Fig. 7 left: Scan of a thin section indicating the locations of the SEM-micrographs 1–4. Right: The images **1** and **2** are situated in the light regions of the zebra dolomite. The micrograph **1** consists almost completely of calcite whereas relicts of the initial dolomite are still observed under high magnification in **2**. The crystal margins clearly exhibit reaction rims that are built up by high-Mg calcite. Micro-

graphs **3** and **4** are in the dark regions of the pattern that had been subjected to a more pronounced dedolomitization compared to the light areas. Another difference is that numerous secondary minerals, such as quartz and feldspar, are present, probably representing detritus from the underlying quartz diorite

Fig. 8 EDS spectra along the margin of a dolomite crystal in the central part of a light zebra layer. The locations of the analyzed points (1–4) are shown in the right SEM micrograph (backscattered). The investigated points progress from the inside of a dolomite crystal into the calcite cement. A successive decrease in Mg content that coincides with an initial increase (1 → 2) and a final drop (3 → 4) of Fe and Mn



(Goldstein and Reynolds 1994). Considering the small size of the fluid inclusions, an estimate of the ice melting temperature was not attempted.

Material for isotope analysis was handpicked from both, light and dark layers of the zebra dolomite, from the late-stage calcite filling in the center of light bands, and from the dolomitic host rocks. The latter was analyzed from a sample that exhibited no zebra texture (Fig. 11a) and from areas outside the actual zebra texture development (Fig. 1b). Rock powder was collected using a scalpel and a dentist drill to avoid any contamination between vein and host rocks. The carbon and the oxygen stable isotope compositions of the samples were analyzed at the Scottish Universities Environmental Research Centre (SUERC) in East Kilbride. The samples were dissolved in phosphoric acid in a water bath at a constant temperature of 70 °C for three days. The resulting CO₂ was collected with an automated sampler and analyzed four times using a VG Optima gas-sourced mass spectrometer with the average of the last three measurements used to establish the $\delta^{18}\text{O}$ and $\delta^{13}\text{C}$ values. The mean analytical reproducibility based on replicates of the internal SUERC laboratory standard MAB-1 was approximately $\pm 0.2\%$. Measured isotope ratios are reported as per mil deviations

relative to the Vienna PeeDee Belemnite (VPDB) using conventional delta notation.

Results

Petrological and microstructural analysis

As the grain size difference between the light and dark bands is a general feature of zebra dolomites (Kelka et al. 2015), the zebra banding is observable at the outcrop scale (Fig. 3). However, it is difficult to discern by transmitted light microscopy (Fig. 4). The dark bands comprise impurity-rich small crystals of dolomite. The dark regions of the sample still contain initial sedimentary features (oid-shaped) and the boundaries of the crystals in these areas appear very dark indicating a high density of impurities (Fig. 4e, f). At the transition from the dark to the light bands, the dolomite crystals increase in size and attain well-developed facets toward the center of the light bands. The light bands comprise impurity-poor euhedral dolomite crystals, and the central part of the layers is frequently filled with calcite crystals that exhibit undulose extinction and twinning (Fig. 5). The latest phase

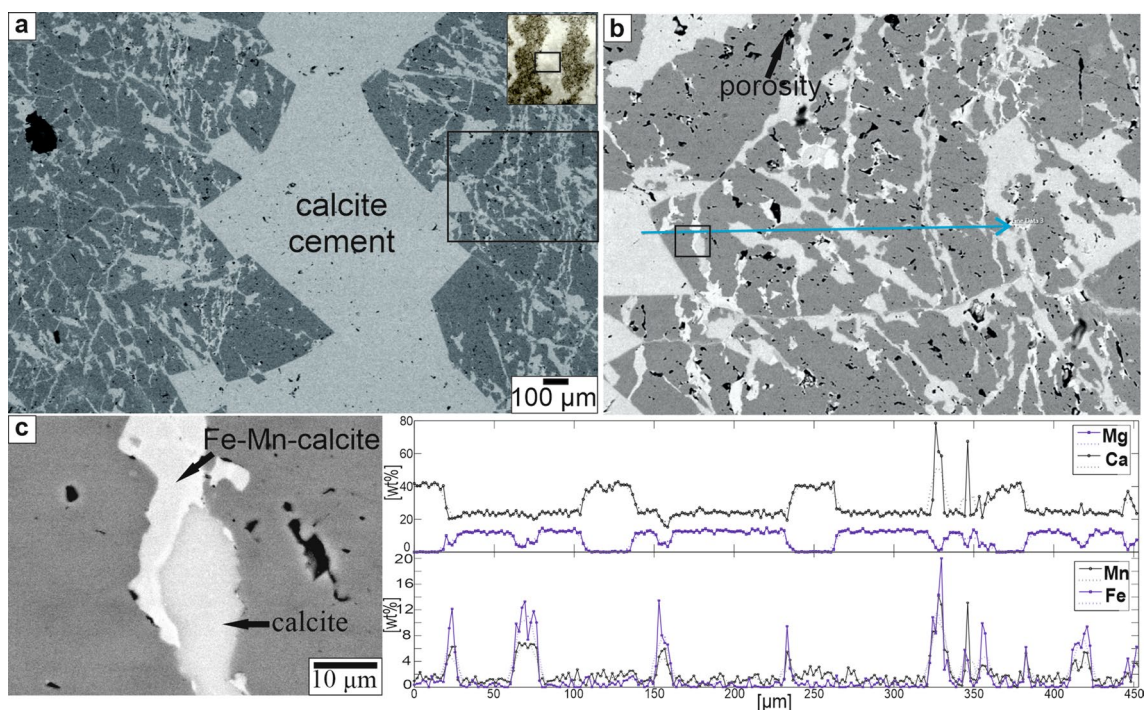


Fig. 9 **a** SEM micrograph (backscattered) of a light zebra layer. The central part of the image shows the calcite cement; along its margins the shape of the dolomite crystals is still visible. Numerous fractures in dolomite are filled with calcite. **b** SEM micrograph (backscattered) of the area marked by the black rectangle in **a**. The fractures are filled with two types of calcite that can be distinguished based on their greyscale value (density). Moreover, the sample has a high porosity. The blue arrow indicates the location and the direction of the EDS

profile in the lower left of the figure. **c** Detailed view (backscattered SEM image) of the area within the black rectangle in **b**. Two calcite phases with a sharp boundary are present in one fracture. The lighter phase consists of (Fe, Mn)-rich, the medium gray of virtually pure calcite. The distribution of the calcite filling, the remaining dolomite, and the concentration of Fe–Mn in one of the calcite phases is shown in the EDS-profile to the lower left of the image

consists of needle-shaped barite crystals that overgrow fine-grained aggregates of calcite (Fig. 5c).

SEM–EDS analysis highlights the occurrence of several mineralogical phases in most samples (Fig. 6): Both dark and light layers are a mix of dolomite and calcite, except for the calcite crystals at the center of the light layers. Within the dark bands, authigenic sulfides pyrite and sphalerite, authigenic arsenides such as cobaltite are present (Fig. 7), along with other authigenic minerals, such as micas, K-feldspar, and quartz. In addition, very small grains of detrital zircon were detected in some of the dark bands. In the center of the light bands, the characteristic shape of the dolomite crystals is preserved but has been partially replaced by calcite, with dolomite crystals surrounded by an inner rim of high (Mn, Fe)-calcite, itself surrounded by pure CaCO_3 (Fig. 8). The same sequence is also encountered both in fractures and along grain boundaries (Fig. 9). Finally, even though in the light areas, some authigenic phases are observed, these are much smaller ($\sim 10 \mu\text{m}$) compared to the larger crystals in the dark areas (up to $200 \mu\text{m}$) (Fig. 10). Under CL (Fig. 11), the light layers and the calcite cement are distinguishable from the dark layers by their brighter luminescence.

Fluid inclusion micro-thermometry

Thirty-nine (39) fluid inclusions were analyzed in the study. 33 were in the light dolomite bands and 6 in the calcite cement (Fig. 12). In the dark bands, observations and measurements of the fluid inclusions were prevented by the opacity caused by numerous impurities. The modal value of the fluid inclusion homogenization temperature (T_h) in the light bands is $116 \text{ }^\circ\text{C}$, with a population ranging from 90 to $280 \text{ }^\circ\text{C}$. The asymmetrical distribution pattern of T_h values indicates that the highest T_h values might reflect thermal resetting at peak burial depth. This is corroborated by the modal value of the T_h measured in the late-stage calcite filling of $305 \text{ }^\circ\text{C}$. Hence, a slightly underestimated crystallization temperature (T_h), for the dolomitization is considered to be ca. $120 \text{ }^\circ\text{C}$, while the maximum crystallization temperature reached by the strata is considered to be preserved by fluid inclusions present in the late-stage calcite and by some reset fluid inclusions in the dolomite, i.e., $305 \text{ }^\circ\text{C}$.

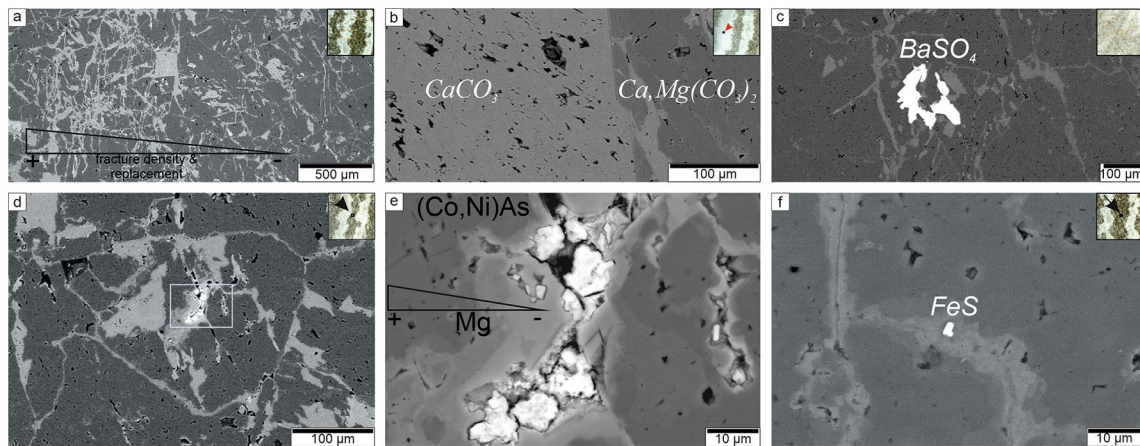


Fig. 10 Selection of SEM-micrographs all obtained in backscattered mode. **a** Micrograph of a light zebra layer. The fracture density and the amount of calcite is highest in the center of the light layer. **b** Micrograph of the boundary between the calcite cement in the center of a light layer. The contact between the two carbonate phases is sharp and an enhanced porosity is observed in the calcite part. **c** Example of a barite aggregate in one of the dark regions of the zebra texture. The precipitation of the Ba phase seems to coincide with the formation of calcite that formed along fractures and grain boundaries. **d** Image of a dark zebra layer. A fracture is visible in the central part of the image that comprises a cluster of high-density material. Cal-

cite can be observed on grain boundaries as well as in the fracture. **e** The area marked by the light-blue rectangle in **d** is shown under high magnification. An EDS analysis revealed that the cluster within the fracture is build up by small crystals of Co–Ni arsenide. A diffusive profile extending from the center of the calcite-filled fracture into the surrounding dolomite coincides with the concentration of Mg in the carbonates, thus indicating progressive dedolomitization. **f** Micrograph of a dark zebra layer showing fractures filled with calcite. This image clearly proves that the dedolomitization progressed from the calcite-filled fracture into the dolomite and also shows that the calcite precipitation coincided with the precipitation of sulfides (pyrite)

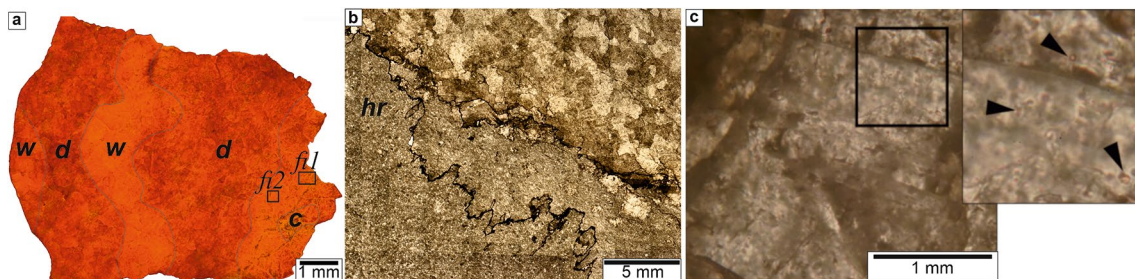


Fig. 11 a Cathodoluminescence image of a zebra dolomite sample. The light layers (w) exhibit a brighter luminescence compared to the dark layers (d) indicating changing redox conditions during the formations of the two phases. In the lower left calcite cement (c) is visible. The rectangles fi1 and fi2 indicate the location of two sets of fluid inclusions analyzed in this study. **b** Fragment of a Zechstein carbonate, not affected by formation of the zebra pattern and subsequent dedolomitization. A clear grain size contrast is obvious, whereas

the boundary between the coarse- and the fine-grained is marked by a stylolite. The fine-grained carbonate in the lower left of the image shows numerous sedimentary features (peloids) and a high impurity concentration whereas less impurities and no sedimentary relicts are present in the coarse-grained region. **c** microphotograph of biphasic primary fluid inclusions (marked with a black arrow on the right-hand side) analyzed in this study

Stable isotope

Oxygen and carbon isotopic ratios were determined for 13 samples from the host rock ($n = 3$: $\delta^{13}\text{C} = [3.20 \text{ to } 3.93]\text{‰ VPDB}$; $\delta^{18}\text{O} = [-10.37 \text{ to } -6.00]\text{‰ VPDB}$), the light bands ($n = 4$: $\delta^{13}\text{C} = [2.04 \text{ to } 3.46]\text{‰ VPDB}$; $\delta^{18}\text{O} = [-12.07 \text{ to } -10.48]\text{‰ VPDB}$); the dark bands ($n = 3$: $\delta^{13}\text{C} = [1.82 \text{ to } 3.57]\text{‰ VPDB}$; $\delta^{18}\text{O} = [-12.43 \text{ to } -10.46]\text{‰ VPDB}$) and the calcite filling in the middle of the light bands ($n = 3$: $\delta^{13}\text{C} = [-3.57 \text{ to } -2.90]\text{‰ VPDB}$; $\delta^{18}\text{O} = [-13.33 \text{ to } -11.84]$

‰ VPDB). Isotope values from the zebra bands are considered collectively to represent the fluid event responsible for the zebra pattern formation, despite the few dedolomitization patches that were not possible to isolate from the bulk material. Data are reported on a $\delta^{18}\text{O}$ vs $\delta^{13}\text{C}$ plot (Fig. 13) and compared to stable isotope ratios obtained from the Hartkoppe rhyolite near Sailauf (Fusswinkel et al. 2014; location on Fig. 1) and from two Zechstein carbonate formations which host mineralization of the Kupferschiefer-type (Bechtel et al. 2000; Bechtel and Püttmann 1991). Considering the

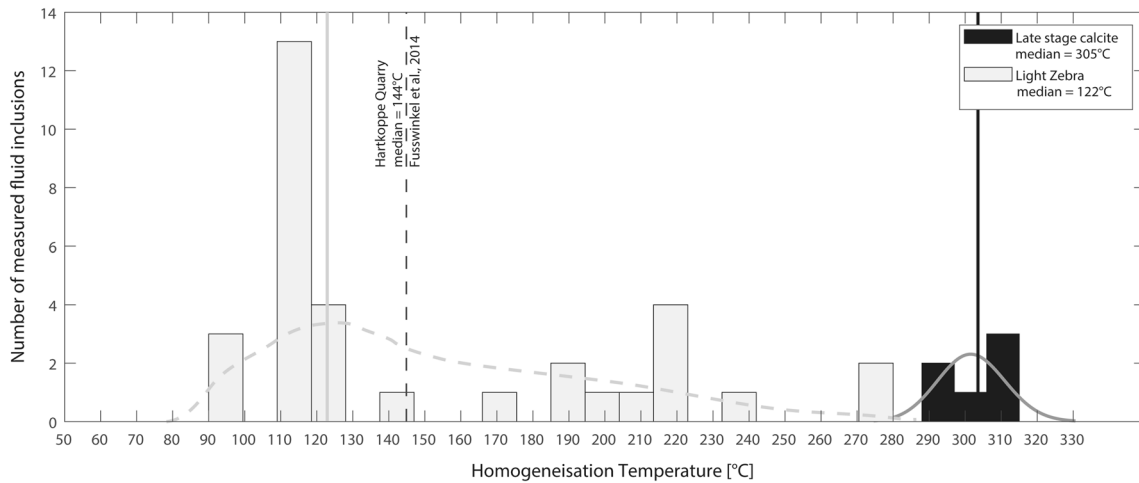


Fig. 12 Histogram showing the homogenization temperature modes of primary fluid inclusions detected in the zebra dolomites from the Falkenberg tunnel. The highest temperatures were recorded within the calcite cement located the central part of the light layers. The other

temperature modes were recorded in fluid inclusion located in the light layer of the zebra texture. The dotted line represents the median value of primary fluid inclusions detected in the calcite vein of the Hartkoppe Quarry near Sailauf

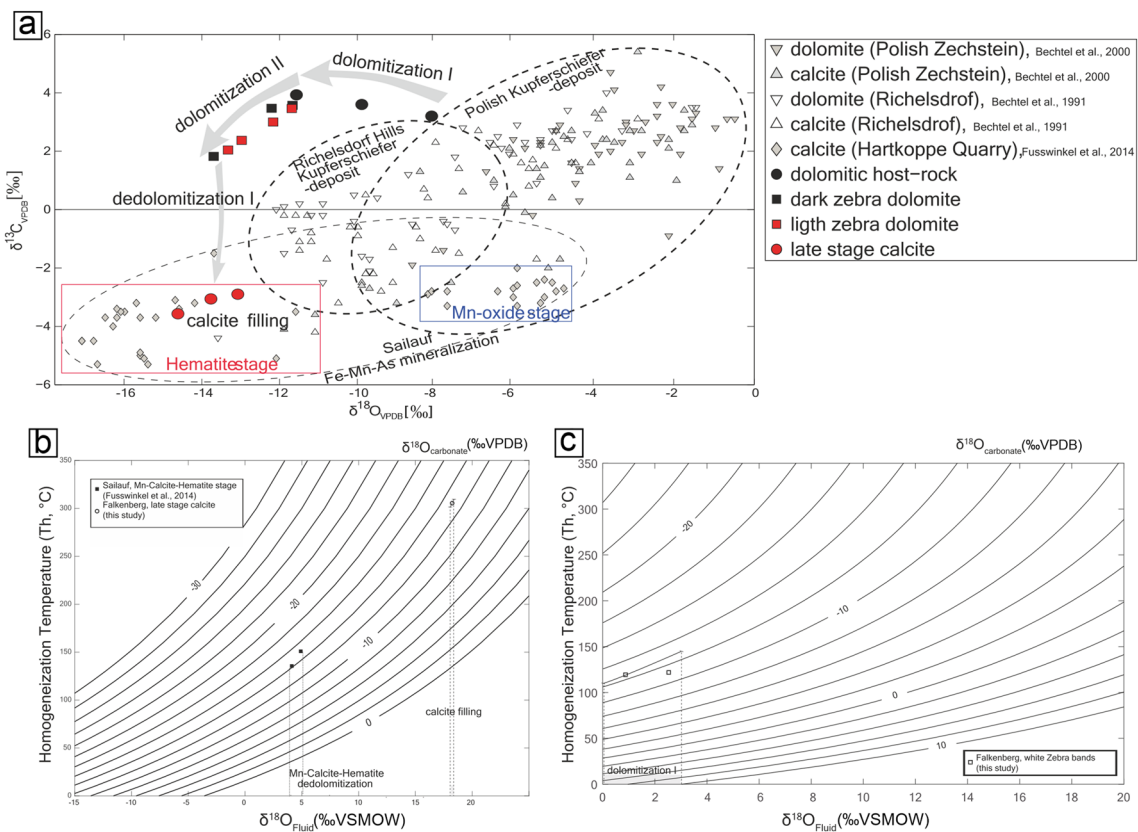


Fig. 13 A Plot of stable isotope ratios of carbon (in ‰ VPDB) versus those of oxygen (in ‰ VPDB) obtained from the Zechstein carbonates in the Falkenberg tunnel compared to published isotope data from the Kupferschiefer deposits in the Richelsdorf Hills (Hesse, Germany) and the Polish Zechstein basin as well as from the Fe–Mn–As mineralization in the Hartkoppe Rhyolite near Sailauf (Spessart). The latter is divided into a Hematite-rich stage and in a Mn oxide

stage, reported within red and blue frames, respectively. Note that the analytical uncertainty is smaller than the size of the points. **B, C** Determination of the $\delta^{18}\text{O}_{\text{VSMOW}}$ values of the precipitating fluids based on the homogenization temperatures (T_h) and the $\delta^{18}\text{O}_{\text{VSMOW}}$ values detected in the carbonates, using the fractionation equation of Kim and O'Neill (1997) for calcite (**B**) and of Horita et al. (2014) for dolomite (**C**)

measured T_h as representative of the minimum fluid temperature at the time of crystallization (Hanor 1980), we can calculate the $\delta^{18}\text{O}$ values for the fluid using fractionation equations (Kim and O'Neil 1997 for calcite; Horita 2014 for dolomite) (Fig. 13b). From our dataset, two distinct groups of fluids are involved in the evolution of the zebra dolomite: (1) a fluid associated with the development of the light layer of the zebra dolostone, that returns a $\delta^{18}\text{O}_{\text{fluid}}$ value of $1 \pm 1\%$ VSMOW (Fig. 13c), and (2) a fluid associated with the late-stage calcite precipitation that yields a $\delta^{18}\text{O}_{\text{fluid}}$ value of 18% VSMOW.

An interpretative sequence of diagenesis and ore genesis

By combining structural and microstructural observations with fluid temperature and isotopic characterization, we propose a sequence which comprised five diagenetic events to have altered the original limestone.

Dolomitization I (dol I)

The first alteration event to affect the limestone was the replacive dolomitization I event. Non-carbonate impurities and original sedimentary features, such as the ooids, were preserved in the dark dolomite bands (Fig. 4e, f). We propose that the signature of the original dolomitizing fluids preserved in the light dolomite bands was likely derived from seawater ($T_h = 122\text{ }^\circ\text{C}$, $\delta^{18}\text{O}_{\text{fluids}} = 0$ to 3%). This suggests that the dolomitization process was related to burial diagenesis, with a temperature consistent with the burial history of the Zechstein group in the basin (Duschl et al. 2016).

Dolomitization II: light zebra layer (dol II)

The large dolomite crystals in the light bands display no record of the initial sedimentary features (e.g., ooids, Fig. 4a), and represent the only phase in which small amounts of sphalerite were identified. These observations support that the zebra texture is related to a secondary dolomitizing event. Unfortunately, the fluid inclusion homogenization temperature could not be measured, limiting the paleofluid characterization. Assuming that the mineralizing fluid was the same as for the dol I (i.e., $\delta^{18}\text{O}_{\text{fluid}} = 0\%$), one can use the measured values of $\delta^{18}\text{O}_{\text{CaCO}_3}$ in the dol II phase to predict that this phase crystallized at a temperature of $220\text{ }^\circ\text{C}$ (using Kim and O'Neil 1997 fractionation equation).

Dedolomitization (dedol)

The dolostones were altered by a fluid flow event that postdated the formation of the zebra texture, as evidenced by the barite veins that crosscut the zebra texture (Fig. 3b),

and the dissolution features present along the central part of the light layers (Fig. 1d). The dedolomitization phase is observed in both, the dark and light bands where dolomite is replaced by Fe–Mn-rich calcite while preserving the initial volume (Fig. 8 phases 1–2–3), which is evidence for a dissolution–precipitation process (Putnis 2009; Centrella et al. 2020). Dedolomitization of the zebra bands clearly progressed along micro-fractures and grain boundaries (Fig. 9a), whereas fracturing and subsequent replacement of dolomite by calcite is more pronounced in the light bands. The calcite filling follows the grain boundaries in the dark bands indicating that the fluid pathways were controlled by the grain boundaries and not by a fracture network (Fig. 10).

The presence of Fe indicates a reducing fluid. Small quantities of pyrite have been found bound to this calcite (Fig. 10f), but unlikely precipitated from the same fluid. The occurrence of this Fe–Mn-rich calcite localized around grain boundaries and inside fractures (Figs. 9, 10) raises the question of whether this could be related to the same fluid system that formed the Mn-rich calcite and hematite present in the area around Sailauf (Fusswinkel et al. 2014). Two possible fluid sources can be considered for this event. First, the isotope measurements can be used to predict a temperature of precipitation of approximately $220\text{ }^\circ\text{C}$ assuming the fluids are seawater. Alternatively, we tentatively combined the T_h measurements reported in Fusswinkel et al. (2014) with the $\delta^{18}\text{O}_{\text{CaCO}_3}$ measurements on the same material and reported in the same study to derive the oxygen isotope value of the fluid responsible for the dedolomitization phase (Fig. 13b). It is noteworthy that doing so means that the $\delta^{18}\text{O}_{\text{CaCO}_3}$ and the T_h values are representative of the same initial fluid–rock interaction event. Under this assumption, the fluids responsible for dedolomitization are characterized by a $\delta^{18}\text{O}_{\text{fluid}}$ value of $4.7 \pm 0.3\%$ (Fig. 13b), hinting toward a slightly evolved basin brine. In such a case, the precipitation temperature is ca. $150\text{ }^\circ\text{C}$.

Late-stage calcite precipitation (cal I)

The light bands of the zebra dolomite are characterized by a median line consisting of a calcite cement of up to 3 mm thick, a small-scale chemical transition with the Mn–Fe calcite produced by the dedol I (Fig. 8). Such a chemical contrast is also observed in the zebra dolostones where pure calcite can be found overprinting Fe–Mn calcite from dedol I. In some samples, macroscopically visible chalcopyrite crystals are found in the late-stage calcite fillings that usually represent zones of microporosity (Fig. 10). From other localities, it was found that the cavernous pores along the median line of the light zebra bands are often filled by calcite or in the proximity of mineralization with chalcopyrite or pyrite (Swennen et al. 2003). The fluid has a very light $\delta^{18}\text{O}_{\text{fluid}}$ value 18% and precipitation occurred at a

very high temperature ($T_h > 300\text{ °C}$), with resulting calcite characterized by a depleted $\delta^{13}\text{C}$ ratio (-4‰). This fluid signature can be interpreted as a highly evolved brine, or as a metamorphic-derived fluid (Beaudoin et al. 2023).

Late-stage barite mineralization

The barite veins within the Zechstein often contain an early dolomite and calcite infill. Chalcopyrite, pyrite, and small amounts of tennantite are often associated with barite veins (Wagner et al. 2010). It is important to note that different phases of barite mineralization occurred in the Spessart. One way to distinguish between the oldest and youngest generation is based on the color and textural appearance. While the older barite generations appear as a uniform aggregate that has a white to slightly yellow color, the younger barite (up to tertiary) exhibits colloform banding with a brown coloration (Lorenz et al. 2018). The age of the older barite mineralization was constrained by the radiometric dating of the texturally older (braunite) and younger (hematite) mineral phases

(Okrusch et al. 2007). U–Th–He-dating reveals that the barite formed between 160 and 145 Ma (Wagner et al. 2010).

Discussion

Fluid system evolution and timing

Based on the analyses presented in this study, we derive a preliminary paragenetic sequence using isotope ratios and the temperatures and fluid characteristics derived from fluid inclusions associated with each phase of carbonate crystallization identified (Fig. 14). First, the Zechstein carbonates were dolomitized during burial (e.g., Davies and Smith 2006) at 120 °C . The depleted $\delta^{18}\text{O}$ values of the dark bands relative to the light bands support a process that involves an interaction with seawater at 220 °C . The local burial history of the basin precludes that the latter temperatures formed due to a high geotherm, especially as there is no volcanic activity reported in the vicinity. Consequently,

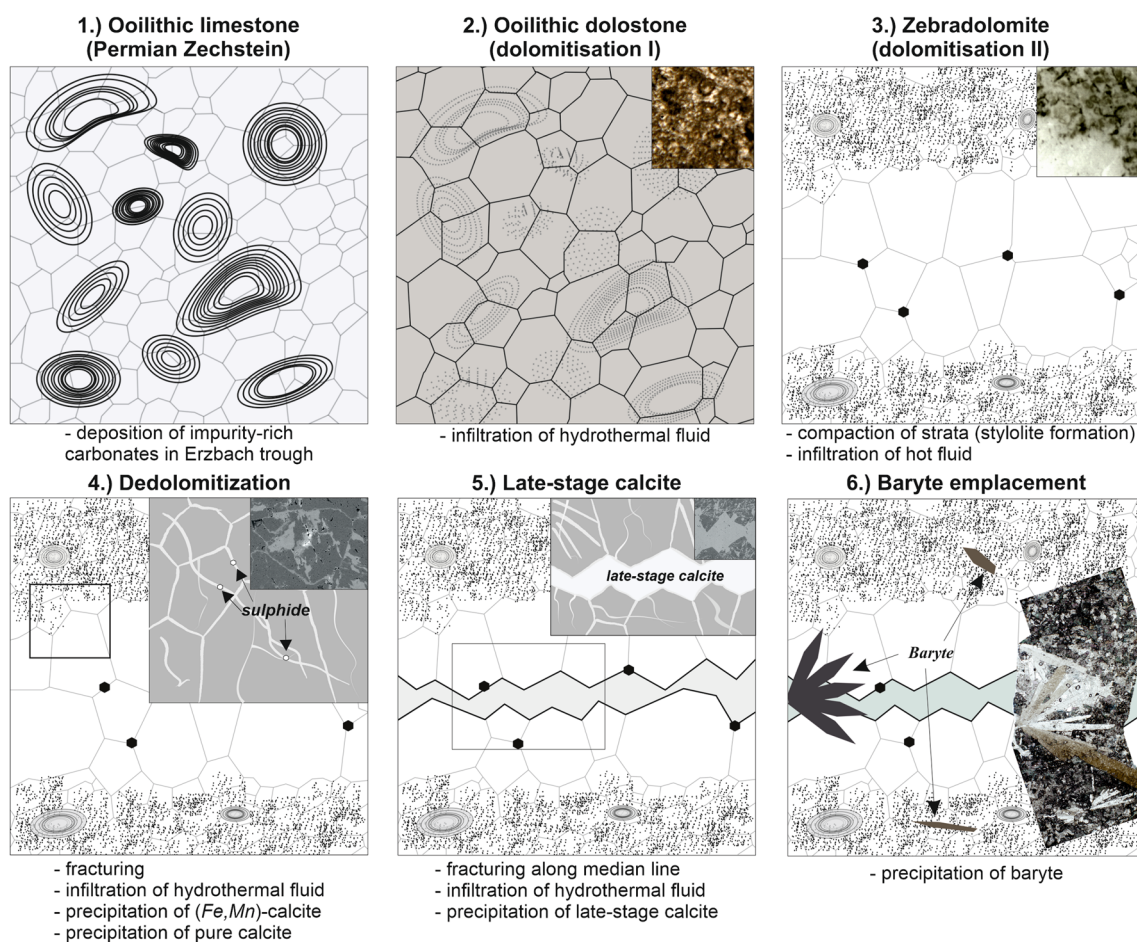


Fig. 14 Schematic sketch of the paragenetic sequence of the Zechstein carbonates from the Falkenberg tunnel based on the microstructural and chemical data obtained in this study

the hypothesis of fluid–rock interactions with local seawater heated to 220 °C is unlikely, so we postulate that the dark layers of the zebra dolomite developed by an interaction with migrating fluids present inside the basin. Subsequently, (Fe, Mn)-calcite, along with pyrite (Fig. 10c, f), and (Co, Ni)-arsenide (Fig. 10d, e) precipitated from a dedolomitizing fluid, that likely represents a slightly evolved seawater at 150 °C (Fusswinkel et al. 2014). Finally, migrating fluids with a temperature of > 300 °C precipitated calcite in the vuggy pores in the light layers of the dolomite. The temperature of precipitation, along with the very light oxygen isotope value of the fluid (> 18‰), support the presence of deep sourced fluids that infiltrated into system.

Comparison of the isotope ratios of the various petrologic phases encountered within the Polish–German Zechstein Basin (Fig. 13) shows that the dolomitization phases dolI and dolII of the zebra dolostones do not coincide with other carbonate phases (Bechtel et al. 1991, 2001). Thus, a link between zebra dolomite formation in the Falkenberg tunnel and the ore fluids in the Polish–German Zechstein basin cannot be established. Therefore, the fluids that formed the hydrothermal ore deposits of the Spessart were either derived from a different source or are the result of different fluid–rock interactions. However, the formation of late-stage calcite falls into a similar geochemical range as that of the hematite stage calcite from the (Fe, Mn, As)-mineralization observed in the Hartkoppe quarry (Fusswinkel et al. 2014), (Figs. 1, 13a). We suggest that a fluid that is similar to the Fe–Mn–As mineralization at Sailauf triggered the dedolomitization event. Consequently, this indicates that the upper boundary for the timing of the zebra dolomite formation is 147.6–136.3 Ma based on dating of the Sailauf mineralization (Hautmann et al. 1999; Okrusch et al. 2007). Our interpretation is that pattern formation in the Falkenberg tunnel has therefore occurred after the deposition of the Zechstein group (Late-Perm) and before the Upper Jurassic.

Even though a hydrothermal fluid system that caused the upwelling of fluids from depth was likely active during the genesis of the zebra pattern, economic mineralization associated with the texture formation cannot be confirmed for the Falkenberg tunnel. Small amounts of ore minerals ((Co, Ni) arsenides) were detected in the light dolomite layers indicating that the fluid contained metals. The hydrothermal solutions caused dedolomitization and precipitation of calcite along grain boundaries and in fractures. Some pyrites also formed from this solution but only in small quantities. Chalcopyrite was observed within larger vugs that had been filled with calcite. It is likely that the barite that overgrows all the previously formed carbonate phases precipitated from this fluid as well.

We propose to pinpoint our paragenetic sequence with absolute ages, based on the findings that the Polish and North German parts of the Zechstein basin were expelling

fluids during the Mesozoic. The ductile Zechstein sedimentary rocks (Schmidt-Mumm and Wolfgramm 2014) later trapped the brines that migrated along normal faults to deep crustal levels during the extension of the basin.

A large-scale fluid system (several hundreds of kilometers) was present in the southern Permian basin and involved fast migrating pulses of fluids, which can be explained by the fast subsidence at the beginning of the late Rotliegend Zechstein periods (260–230 Ma), and that continued until the late Cretaceous when the inversion of the basin occurred (Alderton et al. 2012). This agrees with evidence of post-Variscan hydrothermal activity found in the Spessart that prevailed from the Middle Jurassic to Early Cretaceous in the form of several pulses (Okrusch et al. 2007).

Lessons learned from the formation of Zebra dolomite

The description and the investigation of new zebra dolostones are good opportunities to further discuss the formation models of zebra textures proposed in the literature. For instance, the preservation of primary sedimentary features such as ooids and the contrast in impurity content between the dark and light bands provide evidence for a non-sedimentary origin of the texture, which is similar to that described for the zebra dolomites encountered at the San Vicente mine in Peru (Kelka et al. 2015). Jigsaw-like matching (Merino et al. 2006; Wallace and Hood 2018) of the dark layers surrounding light layers was not observed in the samples from the Falkenberg tunnel. This, together with the change in orientation of approximately 90 degrees of the zebra layering on a decimeter scale (Fig. 1a), indicates that fracturing is unlikely to be the fundamental process of fabric formation.

As outlined in Fig. 14, we propose a two-stage process for the zebra fabric development; dolomitization of the initial limestone was followed by a second dolomitizing event that led to recrystallization and the development of the light bands. To trigger both, the replacement of the initial limestone and the subsequent recrystallization, the fluids must have provided enough *Mg* to maintain the reaction. Saline solutions that were either derived from seawater or from interaction with evaporites are proposed as a potential source of the *Mg*-rich fluids. Our interpretation of the fluid system and diagenetic evolution of the host rock relates the zebra fabric formation to basinal brines with a temperature of ca. 200 °C.

As we have shown, dolomitization of the Zechstein strata in the Falkenberg Tunnel is more pronounced in the dark zebra layers (Fig. 6) leading to a complete replacement of dolomite by calcite in these areas. This may indicate that the initial grain size was very fine in the dark layers resulting in a much larger reactive surface area. Hodson (2006) who

also found that coarser grains were more likely to fracture in response to dissolution experimentally confirmed the correlation between finer grain size and a large reactive surface area. The development of deep cracks in coarse crystalline rocks during dissolution could explain the dense fracture networks in the coarse-grained layers that post-date the fabric development. Dissolution can also be enhanced by compression, for instance during tectonic or diagenetic compaction, and it has been shown that the initial roughness of grain boundaries tends to increase which would further enhance the reactive surface area (Koehn et al. 2006). Furthermore, coarser crystalline aggregates are more susceptible to fracturing as the yield stress drops with decreasing crystal size (Hall 1951; Petch 1953).

Recent models for the formation of zebra dolomites propose that the formation is triggered by considerable volumetric strain in a low-permeable, fluid-saturated rock that leads to the development of material instabilities (Kelka et al. 2017). These instabilities create channels of enhanced permeability with elevated fluid pressure (Veveakis and Regenauer-Lieb 2015). This mechanism is supported by the presence of late-stage calcite in the fractures at the center of the light bands, and the (hydro-)fracture pattern in the dolostone might further indicate the presence of high fluid pressure (Vass et al. 2014).

Conclusion

In this study, we present for the first time an attempt to derive the paragenetic and diagenetic history of zebra fabrics in the dolomites of the Zechstein Group present in the western margin of the Spessart Crystalline Complex. Combining several analytical techniques (optical microscopy, SEM–EDX, CL, FI micro-thermometry, and stable isotope analysis) leads to unraveling a five-phase process consisting of two dolomitization events, followed by dedolomitization event with associated calcite precipitation and, finally, a late-stage calcite and barite crystallization event. Based on our petrographic observations, fracturing as the primary mechanism for producing the zebra pattern is unlikely, and dissolution along the boundaries of sedimentary layers is probably not the primary cause for this process, either. Rather, a continuous supply of reactive solutions that was maintained over a prolonged period is a more plausible explanation for the formation of the light zebra layers. For the zebra dolomites encountered in the Falkenberg tunnel, the underlying fluid system was likely linked to NW–SE striking fault zones (Fig. 2) that represent important structures for Cu–Co–Ni–As ores (Wagner et al. 2010) and explain the abundant barite mineralization in the Spessart (Okrusch et al. 2007).

Moreover, we demonstrate that a deep-seated fluid system was reactivated after the formation of the zebra structures leading to subsequent dedolomitization and replacement of the zebra dolomite by (Mn–Fe)-rich calcite. This fluid percolated through micro-fractures and along grain boundaries, causing the dedolomitizing reaction to be enhanced in the dark bands, which show smaller crystal sizes and thus possess a higher reactive surface area.

In the framework of the western margin of the Spessart, we identified two temporally separated fluid pulses, differing significantly in temperature and isotope characteristics, thus likely representing two chemically different solutions. This finding confirms that the marginal facies of the Zechstein was affected by pulsed upwelling of hot fluids. Our study findings further support the interpretation that the zebra structure is not purely a sedimentary or diagenetic feature, but is a potential indicator for the presence of hydrothermal systems.

Acknowledgements This work has received funding from the European Union's Seventh Framework Programme for research, technological development, and demonstration under Grant agreement no. 316889. We thank the CSIRO DEI-FSP for supporting the continuation of this work. We further thank Tobias Schlegel and Caroline Johnson for the thoughtful review of the manuscript.

Funding Open access funding provided by CSIRO Library Services.

Data availability Data presented in this study is available from the author upon request.

Declarations

Conflict of interest The authors declare no potential conflict of interests.

Open Access This article is licensed under a Creative Commons Attribution 4.0 International License, which permits use, sharing, adaptation, distribution and reproduction in any medium or format, as long as you give appropriate credit to the original author(s) and the source, provide a link to the Creative Commons licence, and indicate if changes were made. The images or other third party material in this article are included in the article's Creative Commons licence, unless indicated otherwise in a credit line to the material. If material is not included in the article's Creative Commons licence and your intended use is not permitted by statutory regulation or exceeds the permitted use, you will need to obtain permission directly from the copyright holder. To view a copy of this licence, visit <http://creativecommons.org/licenses/by/4.0/>.

References

- Alderton DHM, Selby D, Kucha H, Blundell DJ (2016) A multistage origin for Kupferschiefer mineralization. *Ore Geol Rev* 79:535–543. <https://doi.org/10.1016/j.oregeorev.2016.05.007>
- Amstutz GC, El Goresy A, Frenzel G, Kluth C, Moh G, Wauschkuhn A, Zimmermann R (2012) On the Alpine mineralization in western Europe outside the Alps. Springer Science & Business Media, New York, pp 598–606

- Arndt N, Ganino C (2012) Hydrothermal deposits, metals and society: an introduction to economic geology. Springer, Berlin, pp 73–112. https://doi.org/10.1007/978-3-642-22996-1_4
- Aydal D, Polat O, Uslu A, Uslu İ (2008) Locating of the ore bearing zebra dolomites by using Landsat 7 ETM+ and Quickbird satellite data in Hinzir Mountain, Kayseri, Turkey
- Badoux V, Moritz R, Fontboté L (2001) The Mississippi Valley-type Zn-Pb deposit of San Vicente, Central Peru: an Andean syntectonic deposit. Mineral deposits at the beginning of the 21st Century. Proceed Joint 6th Biennial SGA-SEG Mtg, Krakow, Poland, 191–195. <https://doi.org/10.1201/9781003077503-48>
- Beales FW, Jackson SA (1968) Pine Point—a stratigraphic approach. *Can Min Metall Bull* 1968:1–12
- Beaudoin N, Lacombe O, Hoareau G, Callot J-P (2023) How the geochemistry of syn-kinematic calcite cement depicts past fluid flow and assists structural interpretations: a review of concepts and applications in orogenic forelands. *Geological Magazine*. <https://doi.org/10.1017/S0016756822001327>
- Bechtel A, Püttmann W (1991) The origin of the Kupferschiefer-type mineralization in the Richelsdorf Hills, Germany, as deduced from stable isotope and organic geochemical studies. *Chem Geol* 91:1–18. [https://doi.org/10.1016/0009-2541\(91\)90012-G](https://doi.org/10.1016/0009-2541(91)90012-G)
- Bechtel A, Gratzner R, Püttmann W, Oszczepalski S (2000) Geochemical and isotopic composition of organic matter in the Kupferschiefer of the Polish Zechstein basin: relation to maturity and base metal mineralization. *Int J Earth Sci* 89:72–89. <https://doi.org/10.1007/s005310050318>
- Bechtel A, Sun Y, Püttmann W, Hoernes S, Hoefs J (2001) Isotopic evidence for multi-stage base metal enrichment in the Kupferschiefer from the Sangerhausen Basin, Germany. *Chem Geol* 176:31–49. [https://doi.org/10.1016/S0009-2541\(00\)00336-3](https://doi.org/10.1016/S0009-2541(00)00336-3)
- Bjørlykke K (1993) Fluid flow in sedimentary basins. *Sediment Geol* 86:137–158. [https://doi.org/10.1016/0037-0738\(93\)90137-T](https://doi.org/10.1016/0037-0738(93)90137-T)
- Blundell DJ, Karnkowski PH, Alderton DHM, Oszczepalski S, Kucha H (2003) Copper mineralization of the Polish Kupferschiefer: a proposed basement fault-fracture system of fluid flow. *Econ Geol* 98:1487–1495. <https://doi.org/10.2113/gsecongeo.98.7.1487>
- Borg G, Piestrzynski A, Bachmann GH, Puttmann W, Walther S, Fiedler M (2012) An Overview of the European Kupferschiefer Deposits. In: Hedenquist JW, Harris M, Camus F (eds) *Geology and Genesis of Major Copper Deposits and Districts of the World—a tribute to Richard H Sillitoe*, Society of Economic Geologists, Denver, Special Publication 16, pp 455–486
- Centrella S, Beaudoin NE, Derluyt H, Motte G, Hoareau G, Lanari P, Piccoli F, Pecheyran C, Callot JP (2020) Micro-scale chemical and physical patterns in an interface of hydrothermal dolomitization reveals the governing transport mechanisms in nature: case of the Layens anticline, Pyrenees, France. *Sedimentology* 68(2):834–854. <https://doi.org/10.1111/sed.12808>
- Chadam J, Ortoleva P (1990) Morphological instabilities in physico-chemical systems. *Earth Sci Rev* 29(1–4):175–181. [https://doi.org/10.1016/0012-8252\(90\)90035-T](https://doi.org/10.1016/0012-8252(90)90035-T)
- Cramer P, Weinelt W (1978) Erläuterungen zur Geologischen Karte von Bayern 1:25000, Blatt Nr. 5922 –Frammersbach, 137 pp, München (Bayrisches Geologisches Landesamt)
- Cruset D, Cantarero I, Vergés J, John CM, Muñoz-López D, Travé A (2017) Changes in fluid regime in syn-orogenic sediments during the growth of the south Pyrenean fold and thrust belt. *Global Planet Change*. <https://doi.org/10.1016/j.gloplacha.2017.11.001>. (Not cited in text)
- Davies GR, Smith LB Jr (2006) Structurally controlled hydrothermal dolomite reservoir facies: an overview. *AAPG Bull* 90:1641–1690. <https://doi.org/10.1306/05220605164>
- Dewers T, Ortoleva P (1990) A coupled reaction/transport/mechanical model for intergranular pressure solution, stylolites, and differential compaction and cementation in clean sandstones. *Geochim Cosmochim Acta* 54(6):1609–1625. [https://doi.org/10.1016/0016-7037\(90\)90395-2](https://doi.org/10.1016/0016-7037(90)90395-2)
- Diehl SF, Hofstra AH, Koenig AE, Emsbo P, Christiansen W, Johnson C (2010) Hydrothermal zebra dolomite in the Great Basin, Nevada—attributes and relation to Paleozoic stratigraphy, tectonics, and ore deposits. *Geosphere* 6:663–690. <https://doi.org/10.1130/GES00530.1>
- Dill HG (2010) The “chessboard” classification scheme of mineral deposits: mineralogy and geology from aluminum to zirconium. *Earth-Sci Rev* 100:420. <https://doi.org/10.1016/j.earscirev.2009.10.011>
- Dill HG (2012) Diagenetic and epigenetic mineralization in Central Europe related to surfaces and depositional systems of sequence stratigraphic relevance. *Int Assoc Sedimentol Spec Publ* 45:151–182. <https://doi.org/10.1002/9781118485347.ch7>
- Dombrowski A, Okrusch M, Richter P, Henjes-Kunst F, Höhndorf A, Kröner A (1995) Orthogneisses in the Spessart Crystalline Complex, north-west Bavaria: Silurian granitoid magmatism at an active continental margin. *Geol Rundsch* 84:399–411. <https://doi.org/10.1007/s005310050014>
- Duschl F, van den Kerkhof A, Sosa G, Leiss B, Wiegand B, Vollbrecht A, Sauter M (2016) Fluid inclusion and microfabric studies on Zechstein carbonates (Ca2) and related fracture mineralizations—new insights on gas migration in the Lower Saxony Basin (Germany). *Mar Pet Geol* 77:300–322. <https://doi.org/10.1016/j.marpetgeo.2016.06.020>
- Fontboté L, Amstutz GC (1982) Observations on ore rhythmites of the Trzebieńka mine, Upper Silesian-Cracow region, Poland. *Ore genesis: the state of the art*. Springer, Berlin, pp 83–91. https://doi.org/10.1007/978-3-642-68344-2_9
- Fontboté L, Gorzawski H (1990) Genesis of the Mississippi Valley-Type Zn-Pb deposit of San Vicente, Central Peru—geologic and isotopic (Sr, O, C, S, Pb) evidence. *Econ Geol Bull Soc* 85:1402–1437. <https://doi.org/10.2113/gsecongeo.85.7.1402>
- Fontboté L (1993). Self-organization fabrics in carbonate-hosted ore deposits: the example of diagenetic crystallization rhythmites (DCRs). In: *Current research in geology applied to ore deposits*. Proceedings of the Second Biennial SGA Meeting., pp. 11–14
- Fusswinkel T, Wagner T, Wenzel T, Wälle M, Lorenz J (2014) Red bed and basement sourced fluids recorded in hydrothermal Mn-Fe-As veins, Sailauf (Germany): a LA-ICPMS fluid inclusion study. *Chem Geol* 363:22–39. <https://doi.org/10.1016/j.chemgeo.2013.10.026>
- Gasparrini M, Bechthardt T, Boni M (2006) Massive hydrothermal dolomites in the southwestern Cantabrian Zone (Spain) and their relation to the Late Variscan evolution. *Mar Petrol Geol* 23:543–568. <https://doi.org/10.1016/j.marpetgeo.2006.05.003>
- Gast RE (1988) Rifting im Rotliegenden Niedersachsens. *Die Geowiss*. 6:115–122
- Goldstein R, Reynolds T (1994) Systematics of fluid inclusions in diagenetic minerals. *SEPM Soc Sedimentary Geol*. <https://doi.org/10.2110/scn.94.31>
- Hal EO (1951) The deformation and ageing of mild steel. 3. Discussion of Results. *P Phys Soc Lond B64*:47–753. <https://doi.org/10.1088/0370-1301/64/9/303>
- Hanor JS (1980) Dissolved methane in sedimentary brines: potential effect on the PVT properties of fluid inclusions. *Econ Geol* 75:603–609. <https://doi.org/10.2113/gsecongeo.75.4.603>
- Hautmann S, Brander H, Lippolt HJ, Lorenz J (1999) K–Ar and (U+Th)–He chronometry of multistage alteration and mineralisation in the Hartkoppe rhyolite, Spessart. *Germany J Conf Abstr* 4:769
- Hirani J, Bastesen E, Boyce A, Corlett H, Eker A, Gawthorpe R, Hollis C, Korneva I, Rotevatn A (2018) Structural controls on non

- fabric-selective dolomitization within rift-related basin-bounding normal fault systems: Insights from the Hammam Faraun fault, Gulf of Suez, Egypt. *Basin Res* 30:990–1014. <https://doi.org/10.1111/bre.12290>
- Hodson ME (2006) Does reactive surface area depend on grain size? Results from pH 3, 25°C far-from-equilibrium flow through dissolution experiments on anorthite and biotite. *Geochim Cosmochim Acta* 70:1655–1667. <https://doi.org/10.1016/j.gca.2006.01.001>
- Hollis C, Bastesen E, Boyce A, Corlett H, Gawthorpe R, Hirani J, Rotvatn A, Whitaker F (2017) Fault-controlled dolomitization in a rift basin. *Geology* 45:219–222. <https://doi.org/10.1130/G38s394.1>
- Horita J (2014) Oxygen and carbon isotope fractionation in the system dolomite–water–CO₂ to elevated temperatures. *Geochim Cosmochim Acta* 129:111–124. <https://doi.org/10.1016/j.gca.2013.12.027>
- Iriarte E, Lopez-Horgue MA, Schroeder S, Caline B (2012) Interplay between fracturing and hydrothermal fluid flow in the Ason Valley hydrothermal dolomites (Basque-Cantabrian Basin, Spain). *Geol Soc Spec Publ* 370:207–227. <https://doi.org/10.1144/SP370.10>
- Jowett EC (1986) Genesis of Kupferschiefer Cu-Ag deposits by convective flow of Rotliegendes brines during Triassic rifting. *Econ Geol* 81:1823–1837. <https://doi.org/10.2113/gsecongeo.81.8.1823>
- Käding KC (2005) Der Zechstein in der Stratigraphischen Tabelle von Deutschland 2002. *Newsl Stratigr* 41:123–127. <https://doi.org/10.1127/0078-0421/2005/0041-0123>
- Kelka U, Koehn D, Beaudoin N (2015) Zebra pattern in rocks as a function of grain growth affected by second-phase particles. *Front Phys* 3:74. <https://doi.org/10.3389/fphy.2015.00074>
- Kelka U, Veveakis M, Koehn D, Beaudoin N (2017) Zebra rocks: compaction waves create ore deposits. *Sci Rep* 7:14260. <https://doi.org/10.1038/s41598-017-14541-3>
- Kim S-T, O’Neil JR (1997) Equilibrium and nonequilibrium oxygen isotope effects in synthetic carbonates. *Geochim Cosmochim Acta* 61:3461–3475. [https://doi.org/10.1016/S0016-7037\(97\)00169-5](https://doi.org/10.1016/S0016-7037(97)00169-5)
- Koeshidayatullah A, Corlett H, Stacey J, Swart PK, Boyce A, Robertson H, Whitaker F, Hollis C (2020) Evaluating new fault-controlled hydrothermal dolomitization models: insights from the Cambrian Dolomite, Western Canadian Sedimentary Basin. *Sedimentology* 67:2945–2973. <https://doi.org/10.1111/sed.12729>
- Koehn D, Malthe-Sørensen A, Passchier CW (2006) The structure of reactive grain-boundaries under stress containing confined fluids. *Chem Geol* 230:207–219. <https://doi.org/10.1016/j.chemgeo.2006.02.026>
- Leach DL, Taylor RD, Diehl SF, Saltus, R.W. (2010) A deposit model for Mississippi Valley-Type lead-zinc ores, Chapter A of Mineral deposit models for resource assessment. U.S. Geological Survey Scientific Investigations Report 2010–5070–A: 52. <https://doi.org/10.3133/sir20105070A>
- Liu S, Huang W, Jansa LF, Wang G, Song G, Zhang C, Sun W, Ma W (2014) Hydrothermal dolomite in the upper Sinian (upper Proterozoic) Dengying formation, east Sichuan basin, China. *Acta Geologica Sinica (english Edition)* 88:1466–1487. <https://doi.org/10.1111/1755-6724.12312>
- López Horgue MA, Iriarte E, Schroeder S, Caline B, Fernández Mendiola PÁ (2009) An example on the tectonic origin of zebra dolomites: the San Martín beach outcrop (Santoña, North Spain). *Geogaceta* 47:85–88
- Lopez-Horgue MA, Iriarte E, Schroeder S, Fernandez-Mendiola PA, Caline B, Corneillie H, Fremont J, Sudrie M, Zert S (2010) Structurally controlled hydrothermal dolomites in Albian carbonates of the Ason valley, Basque Cantabrian Basin, Northern Spain. *Mar Petrol Geol* 27:1069–1092. <https://doi.org/10.1016/j.marpetgeo.2009.10.015>
- Lorenz J, Schmitt RT, Völker A (2018) Die untertägige Mangan- und Eisenerzgrube „Heinrich“ zwischen Eichenberg und Sailauf im Spessart—später die Grube „Marga“ auf Schwerspat. *Jahresber Mitt Oberrhein Geol Verein* 100:483–508. <https://doi.org/10.1127/jmoggv/100/0014>
- Lorenz J (2018) Die Tunnel zwischen Laufach und Heigenbrücken. Die Jahrhundertbaustelle der Umfahrung des Schwarzkopftunnels: Geologie, Mineralogie, Geschichte, Bau und Technik der neuen Eisenbahntunnel durch den Spessart. ISBN-Nr. 978–3–00–059975–0; 458 pp
- Lugli S, Torres-Ruiz J, Garuti G, Olmedo F (2000) Petrography and geochemistry of the Eugui magnesite deposit (Western Pyrenees, Spain): evidence for the development of a peculiar zebra banding by dolomite replacement. *Econ Geol* 95:1775–1791. <https://doi.org/10.2113/95.8.1775>
- MacDonald AJ, Spooner ETC (1981) Calibration of a Linkam TH 600 programmable heating-cooling stage for microthermometric examination of fluid inclusions. *Econ Geol* 76(5):1248–1258. <https://doi.org/10.2113/gsecongeo.76.5.1248>
- Merino E (2006) Self-accelerating dolomite-for-calcite replacement and displacive zebra veins: dynamics of burial dolomitization. *Geochim Cosmochim Acta* 70:A417–A417. <https://doi.org/10.1016/j.gca.2006.06.839>
- Merino E, Canals A (2011) Self-accelerating dolomite-for-calcite replacement: self-organized dynamics of burial dolomitization and associated mineralization. *Am J Sci* 311:573–607. <https://doi.org/10.2475/07.2011.01>
- Merino E, Canals A, Fletcher RC (2006) Genesis of self-organized zebra textures in burial dolomites: displacive veins, induced stress, and dolomitization. *Geol Acta* 4:383–393
- Morrow DW (2014) Zebra and boxwork fabrics in hydrothermal dolomites of northern Canada: Indicators for dilational fracturing, dissolution or in situ replacement? *Sedimentology* 61:915–951. <https://doi.org/10.1111/sed.12094>
- Muchez P, Heijlen W, Banks D, Bundell D, Boni M, Grandia F (2005) Extensional tectonics and the timing and formation of basin-hosted deposits in Europe. *Ore Geol Rev* 27:241–267. <https://doi.org/10.1016/j.oregeorev.2005.07.013>
- Nielsen P, Swennen R, Muchez PH, Keppens E (1998) Origin of Dinantian zebra dolomites south of the Brabant-Wales Massif, Belgium. *Sedimentology* 45:727–743. <https://doi.org/10.1046/j.1365-3091.1998.00171.x>
- Okrusch M, Richter P (1986) Orthogneisses of the Spessart crystalline complex, Northwest Bavaria: indicators of the geotectonic environment? *Geol Rundsch* 75:555–568. <https://doi.org/10.1007/BF01820631>
- Okrusch M, Weber K (1996) Der Kristallinkomplex Des Vorspessart. *Zgeol Wiss* 24:141–174
- Okrusch M, Lorenz JA, Weyer S (2007) The genesis of sulfide assemblages in the former Wilhelmine Mine, Spessart, Bavaria, Germany. *Can Mineral* 45:723–750. <https://doi.org/10.2113/gscanmin.45.4.723>
- Okrusch M, Weinelt W (1965) Erläuterungen zur Geologischen Karte von Bayern 1: 25 000, Blatt Nr. 5921, Schöllkrippen. 327 pp, Munich (Bayrisches Geologisches Landesamt).
- Okrusch M, Geyer G, Lorenz J (2011) Spessart—Geologische Entwicklung und Struktur, Gesteine und Minerale. Sammlung geologischer Führer, Band 106, 368 pp, Stuttgart (Borntraeger)
- Palinkaš SS, Spangenberg JE, Palinkaš LA (2009) Organic and inorganic geochemistry of Ljubija siderite deposits, NW Bosnia and Herzegovina. *Mineral Dep* 44:893–913. <https://doi.org/10.1007/s00126-009-0249-z>
- Petch NJ (1953) The cleavage strength of polycrystals. *J Iron Steel* 174:25–28
- Putnis A (2009) Mineral replacement reactions. *Rev Mineral Geochem* 70:87–124. <https://doi.org/10.2138/rmg.2009.70.3>
- Radke BM, Mathis RL (1980) On the formation and occurrence of saddle dolomite. *J Sed Res* 50:1149–1168. <https://doi.org/10.1306/212F7B9E-2B24-11D7-8648000102C1865D>

- Rosenbaum J, Sheppard SMF (1986) An isotopic study of siderites, dolomites and ankerites at high temperatures. *Geochim Cosmochim Acta* 50:1147–1150. [https://doi.org/10.1016/0016-7037\(86\)90396-0](https://doi.org/10.1016/0016-7037(86)90396-0)
- Schmidt FP, Friedrich G (1988) Geologic setting and genesis of Kupferschiefer mineralization in West Germany. In: Friedrich, GH, Herzig PM (eds) *Base Metal Sulfide deposits in sedimentary and volcanic environments: proceedings of the DMG-GDMB-SGA-Meeting Aachen, 1985*. Springer, Berlin, pp. 25–59. https://doi.org/10.1007/978-3-662-02538-3_3
- Schmidt-Mumm A, Wolfgramm M (2004) Fluid systems and mineralization in the north German and Polish basin. *Geofluids* 4:315–328. <https://doi.org/10.1111/j.1468-8123.2004.00090.x>
- Shelton KI, Hendry JP, Gregg JM, Truesdale JP, Somerville ID (2019) Fluid circulation and fault- and fracture-related diagenesis in Mississippian synrift carbonate rocks on the northeast margin of the metalliferous Dublin Basin, Ireland. *J Sed Res* 89:508–536. <https://doi.org/10.2110/j.sr.2019.31>
- Sibson RH, Moore JMM, Rankin AH (1975) Seismic pumping—a hydrothermal fluid transport mechanism. *J Geol Soc* 131:653–659. <https://doi.org/10.1144/gsjgs.131.6.0653>
- Słowakiewicz M, Blumenberg M, Więclaw D, Röhling HG, Scheeder G, Hindenberg K, Leśniak A, Idiz EF, Tucker ME, Pancost RD, Kotarba MJ (2018) Zechstein main dolomite oil characteristics in the Southern Permian Basin: I. Polish and German sectors. *Mar Pet Geol* 93:356–375. <https://doi.org/10.1016/j.marpetgeo.2018.03.023>
- Swennen R, Vandeginste V, Ellam R (2003) Genesis of zebra dolomites (Cathedral Formation: Canadian Cordillera Fold and Thrust Belt, British Columbia). *J Geochem Explor* 78:571–577. [https://doi.org/10.1016/S0375-6742\(03\)00065-7](https://doi.org/10.1016/S0375-6742(03)00065-7)
- Swennen R, Dewit J, Fierens E, Muchez P, Shah M, Nader F, Hunt D (2012) Multiple dolomitization events along the Pozalagua Fault (Pozalagua Quarry, Basque-Cantabrian Basin, Northern Spain). *Sedimentology* 59:1345–1374. <https://doi.org/10.1111/j.1365-3091.2011.01309.x>
- Thomassen (2007) Barite and celestite in central East Greenland. Exploration and mining Greenland: Greenland mineral resources—Fact Sheet No.14
- Travé A, Labaume P, Vergés J (2007) Fluid systems in foreland fold-and-thrust belts: an overview from the southern Pyrenees. *Thrust belts and foreland basins*. Springer, Berlin, pp 93–115. https://doi.org/10.1007/978-3-540-69426-7_5
- Vandeginste V, Swennen R, Gleeson SA, Ellam RM, Osadetz K, Roure F (2005) Zebra dolomitization as a result of focused fluid flow in the Rocky Mountains Fold and Thrust Belt, Canada. *Sedimentology* 52:1067–1095. <https://doi.org/10.1111/j.1365-3091.2005.00724.x>
- Vandeginste V, Swennen R, Allaey M, Ellam RM, Osadetz K, Roure F (2012) Challenges of structural diagenesis in foreland fold-and-thrust belts: a case study on paleofluid flow in the Canadian Rocky Mountains west of Calgary. *Mar Pet Geol* 35:235–251. <https://doi.org/10.1016/j.marpetgeo.2012.02.014>
- Vass A, Koehn D, Toussaint R, Ghani I, Piazzolo S (2014) The importance of fracture-healing on the deformation of fluid-filled layered systems. *J Struct Geol* 67:94–106. <https://doi.org/10.1016/j.jsg.2014.07.007>
- Vaughan DJ, Sweeney MA, Friedrich G, Diedel R, Haranczyk C (1989) The Kupferschiefer; an overview with an appraisal of the different types of mineralization. *Econ Geol* 84:1003–1027. <https://doi.org/10.2113/gsecongeo.84.5.1003>
- Veveakis E, Regenauer-Lieb K (2015) Cnoidal waves in solids. *J Mech Phys Solids* 78:231–248. <https://doi.org/10.1016/j.jmps.2015.02.010>
- Wagner T, Lorenz J (2002) Mineralogy of complex Co-Ni-Bi vein mineralization, Bieber deposit, Spessart, Germany. *Miner Mag* 66:385–407. <https://doi.org/10.1180/0026461026630036>
- Wagner T, Okrusch M, Weyer S, Lorenz J, Lahaye Y, Taubald H, Schmitt RT (2010) The role of the Kupferschiefer in the formation of hydrothermal base metal mineralization in the Spessart ore district, Germany: insight from detailed sulfur isotope studies. *Miner Deposita* 45:217–239. <https://doi.org/10.1007/s00126-009-0270-2>
- Wallace MW, Hood A (2018) Zebra textures in carbonate rocks: Fractures produced by the force of crystallization during mineral replacement. *Sediment Geol* 368:58–67. <https://doi.org/10.1016/j.sedgeo.2018.03.009>
- Wallace MW, Both RA, Ruano SM, Hachali PF (1994) Zebra textures from carbonate-hosted sulfide deposits—sheet cavity networks produced by fracture and solution enlargement. *Econ Geol Bull Soc* 89:1183–1191. <https://doi.org/10.2113/gsecongeo.89.5.1183>
- Walther HW (2012) On the Alpidic mineralization of Western Central Europe outside the Alps. *Ore genesis: the state of the art*. Science & Business Media, Berlin, pp 598–606. https://doi.org/10.1007/978-3-642-68344-2_57
- Will TM, Lee S-H, Schmädicke E, Frimmel HE, Okrusch M (2015) Variscan terrane boundaries in the Odenwald-Spessart basement, Mid-German Crystalline Zone: new evidence from ocean ridge, intraplate and arc-derived metabasaltic rocks. *Lithos* 220–223:23–42. <https://doi.org/10.1016/j.lithos.2015.01.018>
- Wood JR, Boles JR (1991) Evidence for episodic cementation and diagenetic recording of seismic pumping events, North Coles Levee, California, USA. *Applied Geochem* 6:509–521. [https://doi.org/10.1016/0883-2927\(91\)90050-Y](https://doi.org/10.1016/0883-2927(91)90050-Y)
- Zeeh S (1995) Complex replacement of saddle dolomite by fluorite within zebra dolomites. *Miner Deposita* 30:469–475. <https://doi.org/10.1007/BF00196406>
- Ziegler PA (1990) *Geological Atlas of Western and Central Europe* (2nd edn). Shell International Petroleum Maatschappij b.v., 238 pp, 252 enclosures